World Electric Vehicle Journal

Article

Frequency Stabilization Based on a TFOID-Accelerated Fractional Controller for Intelligent Electrical Vehicles Integration in Low-Inertia Microgrid Systems

Mohamed Abdelkader [1], Emad M. Ahmed [2,*], Emad A. Mohamed [3,4], Mokhtar Aly [5], Ahmed Alshahir [2], Yousef S. Alrahili [2], Salah Kamel [1], Francisco Jurado [6] and Loai Nasrat [1]

1 Department of Electrical Engineering, Faculty of Engineering, Aswan University, Aswan 81542, Egypt; mohamed.abdelkader07@gmail.com (M.A.); skamel@aswu.edu.eg (S.K.); loainasrat@aswu.edu.eg (L.N.)
2 Department of Electrical Engineering, College of Engineering, Jouf University, Sakaka 72388, Saudi Arabia; aaalshahir@ju.edu.sa (A.A.); y.alrahili@tvtc.gov.sa (Y.S.A.)
3 Department of Electrical Engineering, College of Engineering, Prince Sattam bin Abdulaziz University, Al Kharj 16278, Saudi Arabia; e.younis@psau.edu.sa
4 Aswan Wireless Communications Research Center (AWCRC), Department of Electrical Engineering, Faculty of Engineering, Aswan University, Aswan 81542, Egypt
5 Facultad de Ingeniería, Arquitectura y Diseño, Universidad San Sebastián, Bellavista 7, Santiago 8420524, Chile; mokhtar.aly@uss.cl
6 Department of Electrical Engineering, University of Jaén, 23700 Jaén, Spain; fjurado@ujaen.es
* Correspondence: emamahmoud@ju.edu.sa

Abstract: Microgrid systems face challenges in preserving frequency stability due to the fluctuating nature of renewable energy sources (RESs), underscoring the importance of advanced frequency stabilization strategies. To ensure power system stability in situations where renewable energy significantly contributes to the energy mix, it is essential to implement load frequency controllers (LFCs). Moreover, with the widespread use of electric vehicles (EVs), leveraging battery storage from EVs for microgrid frequency control is becoming increasingly crucial. This integration enhances grid stability and offers a sustainable solution by utilizing renewable energy more efficiently and reducing dependency on traditional power sources. Therefore, this paper proposes an innovative approach to LFCs, using fractional-order control techniques to boost the resilience of the interconnected microgrid systems. The approach centers on a centralized control scheme with a tilt fractional-order integral-derivative featuring an accelerated derivative (TFOID-Accelerated) controller. The accelerated derivative component of this controller is tailored to mitigate high-frequency disturbances, while its tilt feature and fractional integration effectively handle disturbances at lower frequencies. As a result, the proposed controller is expected to efficiently counteract disturbances caused by variability in RESs and/or load changes, achieving a high level of disturbance rejection. Additionally, this paper employs the recent growth optimizer (GO) method for the optimal design of the controller's parameter set, avoiding the need for complex control theories, elaborate disturbance observers, filters, and precise power system modeling. The GO algorithm enhances fractional-order capabilities, offering a robust solution to the challenges of renewable energy variability and demand fluctuations. This is accomplished by optimizing parameters and simplifying the control system design across different microgrid scenarios. The proposed TFOID-Accelerated LFC demonstrates superior performance in enhancing frequency stability and minimizing oscillations compared to existing controllers, including traditional proportional-integral-derivative (PID), PID-Accelerated (PIDA), and tilt-integral-derivative (TID) controllers.

Keywords: energy storage; fractional-order controller; electric vehicles (EV); interconnected microgrid (MG); load frequency control (LFC); renewable energy sources (RESs); vehicle-to-grid (V2G)

Citation: Abdelkader, M.; Ahmed, E.M.; Mohamed, E.A.; Aly, M.; Alshahir, A.; Alrahili, Y.S.; Kamel, S.; Jurado, F.; Nasrat, L. Frequency Stabilization Based on a TFOID-Accelerated Fractional Controller for Intelligent Electrical Vehicles Integration in Low-Inertia Microgrid Systems. *World Electr. Veh. J.* **2024**, *15*, 346. https://doi.org/10.3390/wevj15080346

Academic Editor: Zhaoyun Zhang

Received: 3 July 2024
Revised: 26 July 2024
Accepted: 27 July 2024
Published: 1 August 2024

1. Introduction

1.1. Microgrid Challenges

The rising global energy demand underscores the urgency of transitioning from finite, non-renewable resources like fossil fuels to renewable energy sources (RESs), including wind, solar, and hydroelectric power [1]. These alternatives offer a sustainable solution by significantly reducing CO_2 emissions and reducing the effects of climate change [2,3]. Renewable technologies, particularly wind and solar, provide the added benefits of lower operational costs and local energy production, enhancing energy security and resilience against disruptions [4]. Despite the benefits, integrating RESs into power grids introduces challenges, such as maintaining stability and managing the intermittency of energy production. The shift from traditional power sources contributing to grid inertia to RESs results in increased frequency and voltage fluctuations [5,6]. Tackling these issues is critical for successfully integrating RESs, as highlighted by the International Energy Agency's forecast, which projects significant growth in solar and wind capacity, surpassing traditional energy sources within the next decade [7].

Networks of interconnected microgrids (MGs), known as multi-MG systems, allow power sharing among various MGs, each comprising diverse AC and DC power sources like PV panels, wind turbines, and energy storage units [8]. These systems aim to enhance grid reliability, flexibility, and efficiency, offering benefits like increased power availability and improved system resilience. Despite these advantages, multi-MG systems face challenges, particularly in frequency regulation due to the complexity of coordinating multiple MGs and the variability introduced by RESs and electric vehicles (EVs). Vehicle-to-grid (V2G) technology offers a cutting-edge approach to modern power systems by enabling two-way energy exchange between electric vehicles (EVs) and the grid [9–11]. This system allows EVs to serve as mobile energy storage units, supporting the grid by releasing stored energy during high-demand periods and recharging when demand is low. V2G improves grid stability, supports the integration of renewable energy sources, and provides financial incentives to EV owners through energy transactions. Utilizing the combined capacity of EVs, V2G plays a crucial role in creating a more robust, efficient, and sustainable power system [12]. Several studies in the literature deal with the provision of additional functionalities by EV batteries [13]. For instance, a hierarchical control method has been proposed in [13] to guarantee energy conservation for EVs and handle system stability. The integration of EVs adds another layer of complexity, with their charging and discharging potentially causing fluctuations in power supply and demand. Nonetheless, multi-MG systems represent a promising approach to modernizing the power grid by leveraging the benefits of distributed energy resources and improving grid stability and efficiency.

1.2. Literature Review

In multi-MG systems, load frequency controllers (LFCs) are crucial for maintaining operational frequency within specific ranges and effectively managing power exchanges across interconnected MGs [14]. Traditional LFC methods, including I, PI, and PID controllers, have been applied due to their simple design and ease of implementation. However, these conventional approaches often fail to address contemporary multi-MG systems' demands. To overcome these limitations, advanced controllers incorporating double derivatives (DD), like IDD LFC and PID + DD LFC, along with derivative filters, such as PIDF and PIDDF, have been introduced, offering enhanced performance [15,16]. Optimization algorithms, like the Bacterial Foraging-based Optimizer Algorithm (BFOA), have further refined control parameters, leading to more efficient and self-tuned LFC strategies [17,18]. A novel non-linear PI LFC strategy, optimized with the Dandelion Optimizer algorithm (DO), has been introduced for single-area electrical grids [19]. Meanwhile, the Artificial Rabbit Optimizer algorithm (ARO) has been utilized to refine PI and PID LFC designs for multi-source microgrid systems [20]. Additionally, a dual-controller approach, employing an integrator (I) for LFC and a proportional-integrator (PI) for virtual inertia control (VIC), was optimized using the Particle Swarm Optimizer (PSO) for interconnected grids [21].

Despite their simplicity and cost-effectiveness, these integer-order (IO)-based LFC solutions face limitations in fully addressing frequency fluctuations, exhibit sensitivity to parameter changes, and offer limited design flexibility.

On the other hand, fractional-order (FO)-based control (FOC) schemes, offering enhanced design flexibility over their IO-based control (IOC) versions, have been extensively explored in the literature. For instance, FOPID controllers have been efficiently tuned using the Imperialist-Competitive Algorithm (ICA) [22], while a unique combination of the Teaching-Learning-Based Optimizer and Pattern Searching (hTLBO-PS) has optimized a tilted ID (TID) controller [23]. Further contributions include the application of salp-swarm algorithms for cascaded TID controllers [24] and a combination of particle swarm optimization with genetic algorithms for TID and TIDF controllers aimed at LFC and superconducting magnetic energy storage (SMES) device management [25]. Additionally, hybrid controllers combining FOPID and TID, termed FOTID, have been optimized with the Manta-Ray-Foraging (MRFO) algorithm [26], and a PFOTID controller was developed using an artificial-ecosystem optimizer (AEO) [27]. The MGWO-CS algorithm, a Grey Wolf Optimizer, and a Cuckoo search blend have been crafted to refine TID LFC strategies [28]. The FOPTID+1 LFC method was introduced with parameters fine-tuned via the Global Neighborhood Algorithm (GNA) [14]. Additionally, the Jaya optimization algorithm was utilized to enhance the design of PIDF, TIDF, IPDF, and ITDF LFCs, considering system non-linearities and HVDC connections [29]. The Grey Wolf Optimizer (GWO) was employed to optimize FOPID-Accelerated (FOPIDA) controllers for maritime microgrid frequency regulation, and an intelligent-FOI (iFOI) LFC approach was optimized using the same method [30,31].

Furthermore, in the realm of LFCs, contributions have led to controllers with enhanced degrees of freedom (DOF) by incorporating multiple input signals into their designs. This includes two-DOF LFCs that leverage both frequency and area control errors (ACE), and three-DOF LFCs that additionally consider tie-line power deviations. Notable developments include a 2DOF I/TD controller optimized with the Water-Cycle Algorithm (WCA) [32], cascaded FOPID/FOPI controllers refined with the Chaos-Game Optimizer (CGO) [33], and various others optimized with sophisticated algorithms, each contributing to the field with unique input integration and optimization strategies [33–37]. The I-TPFOD controller was introduced and refined using the Satin Bowerbird Optimizer (SBO), incorporating a novel integral-squared error (NISE) objective function for parameter optimization [38]. Research on redox-flow batteries' (RFB) impact on a five-area interconnected grid's frequency regulation was conducted, proposing the FOPIDN-FOPDN LFC optimized via the Selfish Herd Optimizer (SHO), outperforming the PSO technique [39]. Additionally, a cascaded LFC strategy utilizing FOPIDA-FOIDN control was developed [40], with a hybrid optimization algorithm combining Artificial Gorilla-Troops (AGTO) and Equilibrium Optimization (EO) into the HGTOEO technique for LFC optimization. A COC-PIDF controller was optimized for LFC applications using the Salp Swarm Algorithm (SSA) [41], and the FOPI-IDDF method for solar-thermal generation systems was optimized with the Crow Searching Optimizer (CSA) [42]. In addition, a new cascaded controller based on 1 + TD/FOTIDF was optimized using the Modified Liver Cancer Optimization Algorithm (MLCA) developed in [43].

1.3. Problem Statement and Paper Contribution

In summary, the efficiency of load frequency control (LFC) and the performance of microgrid (MG) systems are greatly affected by the selected LFC strategy and the design methodology of the control system. While there have been advancements in this domain, further research is needed to improve MG responses to fluctuations in renewable energy, utilize EV system batteries, and optimize performance across various regions. Although the Growth Optimizer (GO) algorithm has shown promise in standard tests, it has not yielded the expected results in LFC applications. This paper suggests employing the GO algorithm with the proposed TFOID-Accelerated (TFOID-A) controller to enhance LFC performance. The primary contributions of this paper are as follows:

- A new strategy for optimal fractional-order LFC enhancing the resilience of multi-microgrid systems is developed. The method employs a centralized TFOID-Accelerated controller to manage power output from traditional power stations and electric vehicles. The controller's accelerated derivative structure effectively counters high-frequency disturbances, while its tilt component and fractional integration address low-frequency disturbances.
- The GO technique is used to optimize control parameters for proposed controllers across different interconnected multi-MG systems. This optimizer determines the best settings to achieve optimal system response and stability, considering the constraints of various multi-MG systems.
- The suggested approach leverages installed RESs and EV batteries by concurrently designing the proposed coordinated LFC and EV controllers.
- The evaluation of the proposed method's robustness and effectiveness takes into account a range of anticipated scenarios, RESs, and uncertainties.
- A thorough comparison with controllers from the existing literature demonstrates the superior performance of the proposed controller.

To clarify the main novelty of the current paper, Table 1 is added, and the existing literature is organized into three main categories as follows:

1. **Category 1 (IOC single-loop structure):** Some examples include the I [44–46], PI [20,21], PID [47,48], non-linear PI [19], and Fuzzy PIDD2 [49].
2. **Category 2 (FOC single-loop structure):** Some examples include the FOPID [50,51], TID [26], FOPIDF [52], FOPIDA [30], TFOID [27], and intelligent FOPI [31].
3. **Category 3 (Multi-loop structure):** Some examples include the PD-PI [53], PI-PDF [54], PI-TDF [55], PD-PID [56], FO-IDF [57], 2DOF PID [58], 3DOF TID [59], and FOPI-IDDF [42].

Table 1. Paper contributions comparison with existing control categories in the literature.

References	Controllers	Algorithms	Category	Main Characteristics of Category
[44,45] [21] [20,46] [47,48] [19] [49]	I I, PI PI PID Non-linear PI Fuzzy-PIDD2	ESO with BE, JBO PSO HHO, ARO ICA, ABC DO GBO	IOC-based single-loop structure	Easily implementable Low ability to mitigate disturbance Possess simple single-loop structure Reduced robustness at parametric uncertainty
[50,51] [26] [52] [31] [30] [27]	FOPID TID FOPIDF iFOI FOPIDA TFOID	SCA, MDWA MRFO ICA GWO GWO AEO, SMA	FOC-based single-loop structure	Increased number of tunable parameters Higher flexibility than IOC methods Better mitigation of disturbance Moderate disturbance rejection performance
[53] [54] [57] [55] [56] [42] [58] [59]	PD-PI PI-PDF FO-IDF PI-TDF PD-PID FOPI-IDDF 2DOF PID 3DOF TID	ESMOA DTBO ICA SSA BA CSA TLBO SSA	Multi-loop-based control structures	Higher number of tunable parameters Mitigating both high- and low-frequency disturbance Highest in design flexibility Enhanced performance compared to IOC and FOC single-loop methods
Proposed	Centralized TFOID-Accelerated	Growth Optimizer (GO)	Single-loop modified FOC	Including tilt component and fractional integration address low-frequency disturbances Including accelerated derivative structure effectively counters high-frequency disturbances Centralized single controller for LFC and EV control Proving better possibility for rejecting disturbances

Table 1. *Cont.*

References	Controllers	Algorithms	Category	Main Characteristics of Category
Proposed	Centralized TFOID-Accelerated	Growth Optimizer (GO)	Single-loop modified FOC	Coordinated LFC and EV control in the design process of the optimum controller Applies recently developed powerful Growth Optimizer (GO) algorithm Simultaneous determination of optimized parameter set of controllers in both areas

1.4. Paper Organization

The remainder of the paper is arranged as follows: Section 2 presents the overall multi-MG structure and modeling. Section 3 details the development of the proposed TFOID-Accelerated controller. Section 4 provides the proposed GO-based optimal design of the proposed TFOID-Accelerated controller. The results and their comparisons are provided in Section 5. The paper concludes with the findings presented in Section 6.

2. Overall Structure and Model of Studied Power System

2.1. Overall Structure Description

The literature presents various case studies of electrical interconnected power systems, such as the single-area case, two-area case, three-area case, and so on. Among these case studies, the two interconnected areas case study has been widely investigated in the literature. Therefore, it is focused on here and employed as a case study to verify our proposed controller and design algorithms. The power system is considered to have two AC-line-based interconnections, and each area facilitates the integration of EVs and various RESs. The overall structure and connected elements in each area are shown in Figure 1. It is assumed that RESs are shared among the two areas, and EVs are equally distributed in the two areas. In the first area (area *a*), a PV plant is installed, and the second area (area *b*) contains a wind plant. Thermal non-reheat generation units are installed in each area. Moreover, each area contains its connected electrical loads.

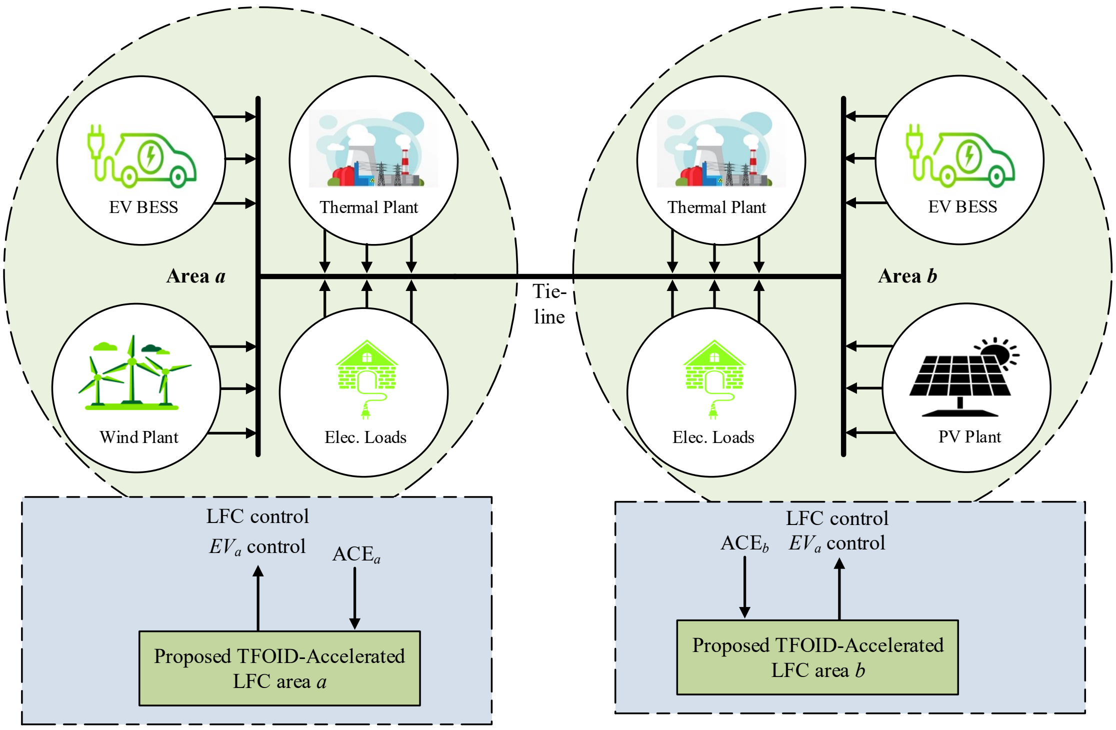

Figure 1. Overall structure description for studied system's elements.

The LFC system performs the generation-loading power balance to minimize deviations in the areas' frequency and tie-line power among them. In particular, LFCs maintain frequency deviation in area a Δf_a, frequency deviation in area a Δf_b, and tie-line power deviation between areas ΔP_{tie} at their minimum values. Hence, improvements in system stability, availability, and disturbance rejection are obtained. In balanced conditions, the generated powers from sources have to be equal to the connected loads, and the LFC has to adjust them very fast to enhance the system performance and stability. Usually, the area control errors ($ACEs$) are employed as feedback error signals for the LFC (here, ACE for area a is ACE_a, and ACE for area b is ACE_b) and are the inputted error signals for the LFC. In the following, the transfer function (TF) models for each individual part are presented and followed by the complete state-space model (SSM).

2.2. EV Model Description

The costly installation of energy storage systems (ESSs) has motivated the employment of EVs battery ESSs (BESSs) for performing additional functionalities in power grids. The vast development and replacement of EVs in the transport sector have enriched the area with more research trends. Thence, with the fast response of lithium-ion BESS and the high EV number in the future, the vehicle-to-grid (V2G) concept has found wide acceptance. BESS is achieved in power systems using EVs' BESSs without adding costs for separate ESS devices. Recent developments in bidirectional DC/AC and DC/DC power converters have facilitated the flexible V2G operation. Accordingly, EVs' BESSs are charged and/or discharged according to the LFC commands and requirements of power system operation scenarios. This, in turn, can lead to enhancing LFC performance and operation, in addition to improvements in system installation costs, efficiency, dynamics, and reliability.

Conventional EV models are based on using first-order TF to model V2G systems. However, they do not consider the internal state of charge (SOC) and voltages/currents of EVs' BESSs. Various elements' models are detailed in Figure 2, in which the used V2G model is shown in each area. The widely used Nernst equations express the dependency of EVs' BESSs open-circuit voltage (V_{oc}) with EVs' BESSs SOC (in particular), $V_{oc}(SOC)$, represented (V_{oc} at different SOC) as follows [27]:

$$V_{oc}(SOC) = V_{nom} + S\,\frac{RT}{F} In\left(\frac{SOC}{C_{nom} - SOC}\right) \tag{1}$$

where V_{nom} is the EVs' BESSs nominal voltages, and C_{nom} is the EVs' BESSs nominal capacities (in Ah), whereas S is the sensitivity of V_{oc} and SOC of the EVs' BESSs. Furthermore, R is the gas constant, F is the Faraday constant, and T stands for the operating temperature.

2.3. PV Plant Representation

Although improved and low-cost PV technologies have widened PV installation plans, the effects of environmental factors represent big issues for PV systems. The variable operating temperature with solar irradiance levels makes the generated PV plant power vary from time to time during the day. These variations are the main cause of PV power intermittency. For maximizing PV plant power generation, MPPT algorithms are responsible for preserving continuous tracking for optimum operating points for maximizing power extraction from PV plants. However, this leads to continuous variations and unbalance between generation powers and loading levels. Thanks to the recent power electronics conversion system, fast response and proper integration of PV powers can be injected into AC power grids.

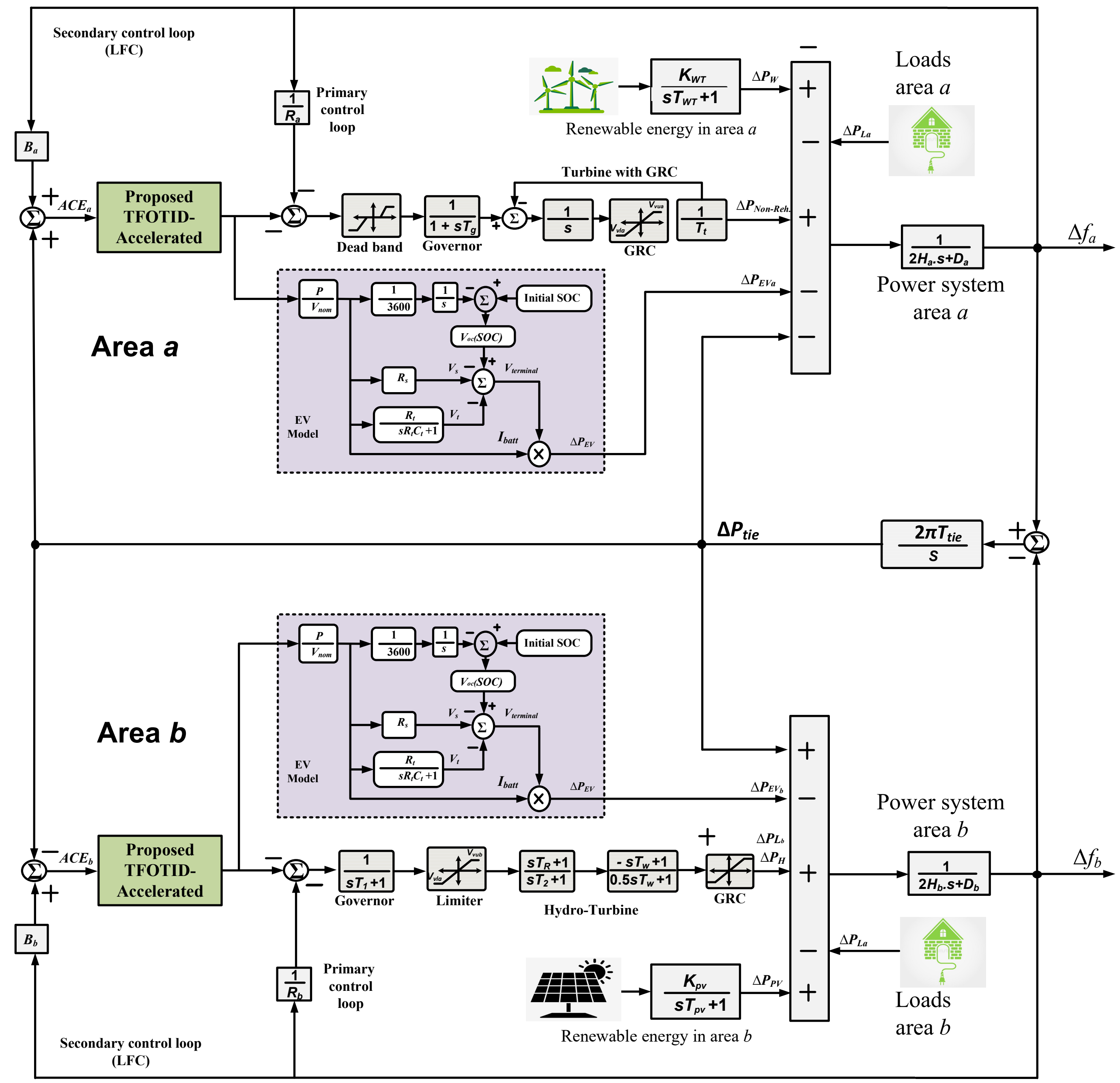

Figure 2. Representation of complete system's elements modeling for considered two-areas power system.

The use of power electronics made PV plants lack the inertia of conventional generation, which is responsible for preserving continuous stable power system frequency control. In addition, the difficulty in predicting PV power generation represents another issue. This, in turn, contributes to having stability-related problems that require robust and efficient LFC, especially with the expected high penetration levels in the future. The generated PV power can be expressed as [26]:

$$P_{PV} = \eta \Phi_{solar} S[1 - 0.005(T_a - 25)] \tag{2}$$

where η denotes the panels' conversion efficiency (in %), Φ_{solar} denotes the solar irradiance level (in W/m^2), S denotes the installation occupied area (in m^2), and T_a denotes the operating temperature (in °C). The PV power generation model based on realistic generated power implementation can be constructed using the presented models in [26].

2.4. Wind Plant Representation

Similar to PV plants, the output power from wind turbines depends on the available wind speed and the employed control method to extract the maximum power from the wind. The extracted mechanical power by wind turbines shows high fluctuation levels. Based on [27], it can be expressed as:

$$P_{wind} = \frac{1}{2}\rho A_r C_p V_w^3 \tag{3}$$

where ρ denotes the air density (kg/m^3), A_r denotes the swept area (m^2), C_p denotes the power coefficient, and V_w represents the wind speed (m/s). An existing realistic data-based wind turbine generation model is implemented based on the model from [26].

The power coefficient C_p depends on the tip-speeds ratio λ and the blades' pitch angle β (denoted as $C_p(\lambda, \beta)$), in which an indicator of the exploited wind power by a particular turbine is used. For $C_p(\lambda, \beta)$, it is defined as [60]:

$$C_p(\lambda, \beta) = 0.5(\lambda_i - 0.022\beta^2 - 5.6)e^{-0.17\lambda_i} \tag{4}$$

Also, λ_i and λ are defined as [60]:

$$\lambda_i = \frac{3600 \times R}{1609 \times R} \tag{5}$$

$$\lambda = \frac{\omega_B \times R}{V_W} \tag{6}$$

This model is used to express the variable extracted wind power with wind speed variations. It is modeled in Matlab with the complete system model. Then, the remaining inverter system and filtering stage is represented as a first-order TF as presented in [60]. The wind system TF $G_{WT}(s)$ is defined as [60]:

$$G_{WT}(s) = \frac{K_{WT}}{T_{WT}s + 1} \tag{7}$$

where K_{WT} denotes the TF model gain for the wind plant and T_{WT} denotes the TF time constant.

2.5. Representations of Thermal and Hydraulic Generators and Grid

Firstly, the thermal plant TF representation is defined based on the governor TF $G_g(s)$, and the turbine TF $G_t(s)$. The various existing non-linearities of the generation rate constraint (GRC) and governor's dead band (GDB) are included. The definition of $G_t(s)$ and $G_g(s)$ TFs are implemented as follows:

$$G_g(s) = \frac{1}{T_g s + 1} \tag{8}$$

$$G_t(s) = \frac{1}{T_t s + 1} \tag{9}$$

The overall thermal plant TF $G_T(s)$ is obtained by combining $G_t(s)$ and $G_g(s)$ as follows:

$$G_T(s) = \frac{1}{T_g s + 1} \cdot \frac{1}{T_t s + 1} \tag{10}$$

Secondly, the hydraulic turbines' performance is determined by the water compressibility, inertia, and pipe wall elasticity. By 1977, recommendations of the IEEE committee for mathematically representing hydraulic turbines were released. Water flowing through the penstock pipes is assumed to be a non-compressible fluid and the water's velocity is proportionate to the gate valve. The velocity of water in penstock pipes is defined as in [43]:

$$U = K_u \cdot G \cdot \sqrt{H_g} \frac{1}{T_t s + 1} \tag{11}$$

where U, H_g, and G denote the proportionality constant, the hydraulic heads, and the position of the gate valve, respectively. The extracted mechanical power by turbine P_m is defined as [43]:

$$P_m = K_p \cdot H_g \cdot U \tag{12}$$

The time elapsed by water to travel over the L length within the conduit with a velocity of U_0 and gravity acceleration of a_g is defined as;

$$T_w = \frac{LU_0}{a_g H_0} \tag{13}$$

A common representation of hydraulic plants is the mode of use of the governor's TF $G_{gh}(s)$, the droop-related compensation TF $G_{gh}(s)$, and the penstock turbine TF $G_{th}(s)$. The overall hydraulic turbine TF $G_h(s)$ representation is defined as follows [60]:

$$G_h(s) = \frac{1}{T_1 s + 1} \cdot \frac{T_R s + 1}{T_2 s + 1} \cdot \frac{-T_w s + 1}{0.5 T_w s + 1} \tag{14}$$

Thirdly, normal modeling of the power system's grid is made by using the first-order-based TF $G_{px}(s)$ as follows:

$$G_{px}(s) = \frac{1}{2H_x s + D_x} \tag{15}$$

where H_x denotes the inertial constant and D_x denotes the damping constant of each considered area.

2.6. Complete System Representation

The aforementioned dynamical models for each element in the studied power system are employed to develop a complete system model for the two-area system. The system's model in Figure 2 contains the different connected elements in both areas. An appropriate way to linearize the system is the state-space representations of dynamical systems. It involves the linearization of the system around the operating point. General model representations can be expressed as:

$$\dot{x} = Ax + B_1 \omega + B_2 u \tag{16}$$

$$y = Cx \tag{17}$$

where $\dot{x}$ denotes the first derivative of x, which represents the state variables vector. A represents the parameters matrix of the x states. y denotes the output states' vector and C represents its model vector to define the output signals. ω denotes the disturbances vector, and B_1 is its parameters matrix. Moreover, u denotes the control variables' vector, and B_2 is its parameters matrix. The vectors (x and ω) are defined as:

$$x = \begin{bmatrix} \Delta f_a & \Delta P_{ga} & \Delta P_{ga1} & \Delta P_{WT} & \Delta f_b & \Delta P_{gb} & \Delta P_{gb1} & \Delta P_{gb2} & \Delta P_{PV} & \Delta P_{tie,ab} \end{bmatrix}^T \tag{18}$$

$$\omega = \begin{bmatrix} \Delta P_{la} & P_{WT} & \Delta P_{lb} & P_{PV} \end{bmatrix}^T \tag{19}$$

From the control side, the variables employed for controlling the system include the ACE controller outputs (ACE_a and ACE_b) and the EVs participation powers (ΔP_{EVa} and ΔP_{EVb}). The control variables related vector is defined as:

$$u = \begin{bmatrix} ACE_a & \Delta P_{EV_a} & ACE_b & \Delta P_{EV_b} \end{bmatrix}^T \quad (20)$$

Based on various developed models, the parameters matrices A, B_1, B_2, and C of the model in (16) are derived from the various elements' models as in Figure 2 as follows:

$$A = \begin{bmatrix} -\frac{D_a}{2H_a} & \frac{1}{2H_a} & 0 & \frac{1}{2H_a} & 0 & 0 & 0 & 0 & 0 & -\frac{1}{2H_a} \\ 0 & -\frac{1}{T_t} & \frac{1}{T_t} & 0 & 0 & 0 & 0 & 0 & 0 & 0 \\ -\frac{1}{R_a T_g} & 0 & -\frac{1}{T_g} & 0 & 0 & 0 & 0 & 0 & 0 & 0 \\ 0 & 0 & 0 & -\frac{1}{T_{WT}} & 0 & 0 & 0 & 0 & 0 & 0 \\ 0 & 0 & 0 & 0 & -\frac{D_b}{2H_b} & \frac{1}{2H_b} & 0 & 0 & \frac{1}{2H_b} & \frac{1}{2H_b} \\ 0 & 0 & 0 & 0 & \frac{2T_R}{R_b T_1 T_2} & -\frac{2}{T_w} & \frac{2T_2+2T_w}{T_2 T_w} & \frac{2T_R-2T_1}{T_1 T_2} & 0 & 0 \\ 0 & 0 & 0 & 0 & -\frac{T_R}{R_b T_1 T_2} & 0 & -\frac{1}{T_2} & \frac{T_1-T_R}{T_1 T_2} & 0 & 0 \\ 0 & 0 & 0 & 0 & -\frac{1}{R_b T_1} & 0 & 0 & -\frac{1}{T_1} & 0 & 0 \\ 0 & 0 & 0 & 0 & 0 & 0 & 0 & 0 & -\frac{1}{T_{PV}} & 0 \\ 2\pi T_{tie,eq} & 0 & 0 & 0 & -2\pi T_{tie,eq} & 0 & 0 & 0 & 0 & 0 \end{bmatrix} \quad (21)$$

$$B_1 = \begin{bmatrix} -\frac{1}{2H_a} & 0 & 0 & 0 \\ 0 & 0 & 0 & 0 \\ 0 & 0 & 0 & 0 \\ 0 & \frac{K_{WT}}{T_{WT}} & 0 & 0 \\ 0 & 0 & -\frac{1}{2H_b} & 0 \\ 0 & 0 & 0 & 0 \\ 0 & 0 & 0 & 0 \\ 0 & 0 & 0 & 0 \\ 0 & 0 & 0 & \frac{K_{PV}}{T_{PV}} \\ 0 & 0 & 0 & 0 \end{bmatrix}, \quad \text{and} \quad B_2 = \begin{bmatrix} 0 & -\frac{1}{2H_a} & 0 & 0 \\ 0 & 0 & 0 & 0 \\ -\frac{1}{T_g} & 0 & 0 & 0 \\ 0 & 0 & 0 & 0 \\ 0 & 0 & 0 & -\frac{1}{2H_b} \\ 0 & 0 & \frac{2T_R}{T_1 T_2} & 0 \\ 0 & 0 & -\frac{T_R}{T_1 T_2} & 0 \\ 0 & 0 & -\frac{1}{T_1} & 0 \\ 0 & 0 & 0 & 0 \\ 0 & 0 & 0 & 0 \end{bmatrix} \quad (22)$$

$$C = \begin{bmatrix} 1 & 0 & 0 & 0 & 0 & 0 & 0 & 0 & 0 & 0 \\ B_a & 0 & 0 & 0 & 0 & 0 & 0 & 0 & 0 & 1 \\ 0 & 0 & 0 & 0 & 1 & 0 & 0 & 0 & 0 & 0 \\ 0 & 0 & 0 & 0 & B_b & 0 & 0 & 0 & 0 & -1 \end{bmatrix} \quad (23)$$

The parameters of the implemented two-area case study are summarized in Table 2.

Table 2. Mathematical model parameters for different areas.

Parameters	Symbols	Area *a*	Area *b*
Nominal power system size	P_{rx} (MW)	1200	1200
Droop gain	R_x (Hz/MW)	2.4	2.4
Frequency bias	B_x (MW/Hz)	0.4249	0.4249
Valve gate limit (minimum)	$V_{g\,\min}$ (p.u.MW)	0.5	0.5
Valve gate limit (maximum)	$V_{g\,\max}$ (p.u.MW)	0.5	0.5
Thermal governor time constant	T_g (s)	0.08	-

Table 2. *Cont.*

Parameters	Symbols	Area *a*	Area *b*
Thermal turbine time constant	T_t (s)	0.3	-
Hydraulic governor time constant	T_{s1} (s)	-	41.6
Hydraulic transient droop time constant	T_{s2} (s)	-	0.513
Hydraulic governor reset times	T_{s3} (s)	-	9.6
Water starting time of hydraulic turbines	T_w (s)	-	1
Area's inertia constant	H_x (p.u.s)	0.0833	0.0833
Area's damping coefficient	D_x (p.u./Hz)	0.00833	0.00833
PV transfer function time constant	T_{pv} (s)	-	1.3
PV transfer function gain	K_{pv}	-	1
Wind transfer function time constant	T_{wT} (s)	1.5	-
Wind transfer function gain	K_{WT}	1	-
EV numbers in each area	-	150,000	150,000
EV participation	-	5%	5%
Battery state of charges	SOC	95%	95%

3. Development of Proposed TFOID-Accelerated Controller

3.1. LFC Based on FOC Method

As clarified in the Section 1, IOC methods using I, PI, and PID have been widely provided in the literature as simple control methods. They benefit from simple design and implementation procedures. Figure 3 presents the three main IOC methods reported in the literature. The TF representations for the IOC-based LFC can be summarized as follows:

$$C_I(s) = \frac{Y(s)}{E(s)} = \frac{K_i}{s} \tag{24}$$

$$C_{PI}(s) = \frac{Y(s)}{E(s)} = K_p + \frac{K_i}{s} \tag{25}$$

$$C_{PID}(s) = \frac{Y(s)}{E(s)} = K_p + \frac{K_i}{s} + K_d\, s \tag{26}$$

$$C_{PIDA}(s) = \frac{Y(s)}{E(s)} = K_p + \frac{K_i}{s} + K_d\, s + K_a\, s^2 \tag{27}$$

where K_p, K_i, K_d, and K_a are the tunable gains parameters for the proportional-term, integral-term, differential-term, and accelerated-term, respectively. Despite their simplicity in design and implementation, they showed lower performance in modern power grid systems due to the existing high disturbances.

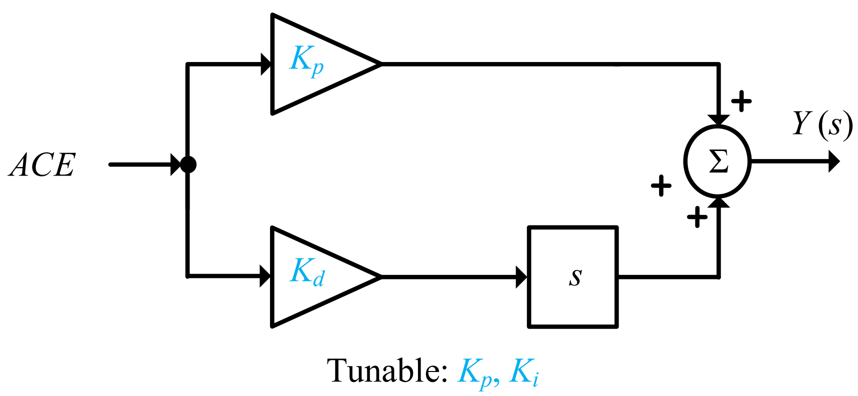

(**a**)

Figure 3. *Cont.*

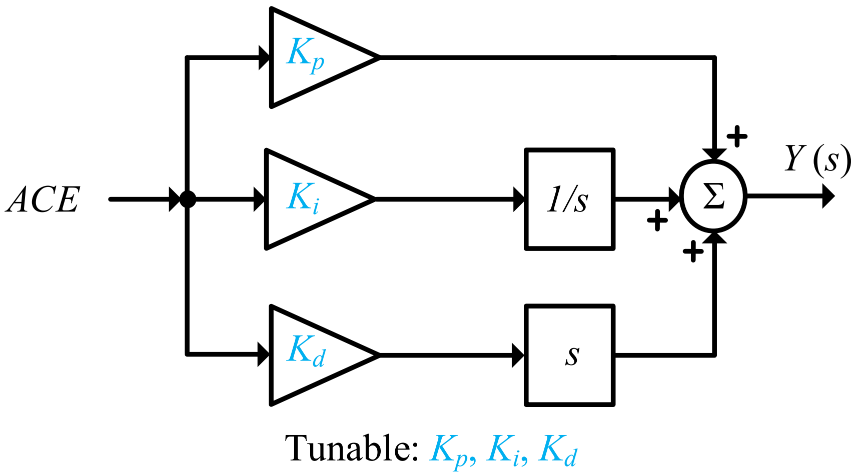

(**b**)

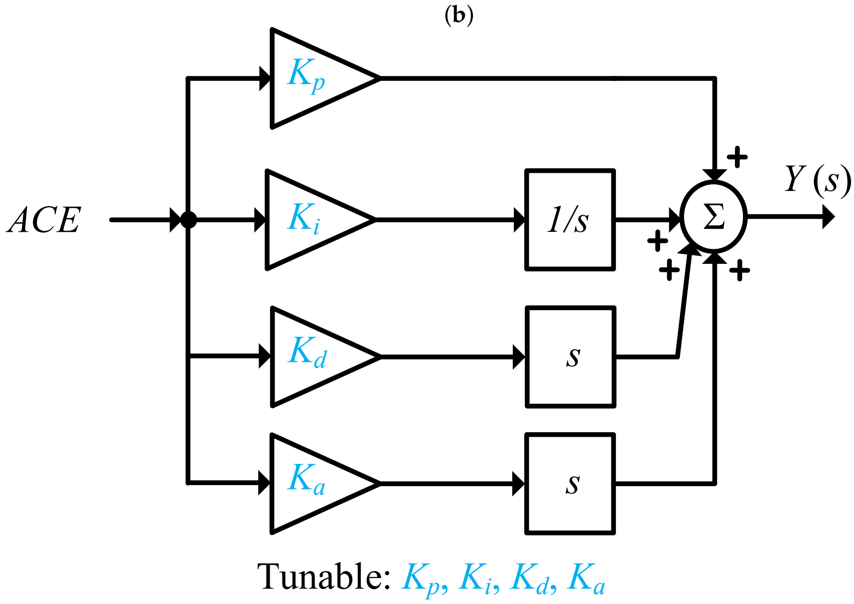

(**c**)

Figure 3. IOC-based LFCs block diagrams with tunable parameters. (**a**) PI control; (**b**) PID control; (**c**) PIDA control.

Thence, research and industry concerns are looking forward to applying FOC methods in LFC to overcome IOC problems. The FOC methods provide more flexibility due to including extra FO operators in their TFs. The FOC-based I, PI, and PID, namely, FOI, FOPI, and FOPID, respectively, are shown in Figure 4. The TF representations for the FOC-based LFC can be summarized as follows:

$$C_{FOI}(s) = \frac{Y(s)}{E(s)} = \frac{K_i}{s^{\lambda}} \tag{28}$$

$$C_{FOPI}(s) = \frac{Y(s)}{E(s)} = K_p + \frac{K_i}{s^{\lambda}} \tag{29}$$

$$C_{FOPID}(s) = \frac{Y(s)}{E(s)} = K_p + \frac{K_i}{s^{\lambda}} + K_d\, s^{\mu} \tag{30}$$

where λ and μ are FOC additional FO operators in addition to the conventional tunable parameters K_p, K_i, and K_d. They have demonstrated more flexibility with a wider range in handling disturbances. Compared to the IOC-based LFC, the FOC-based PID is capable of simultaneously handling several control objectives at a wider dynamical operating range.

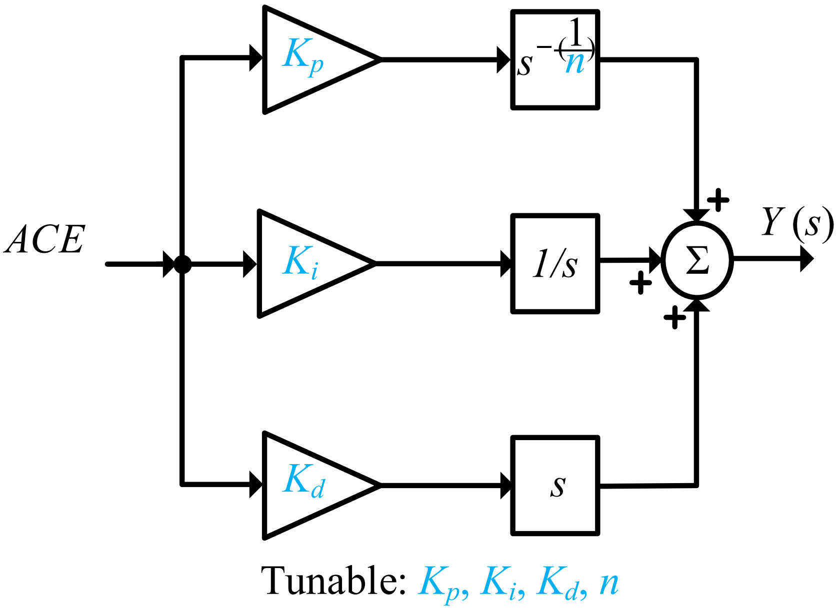

(**a**)

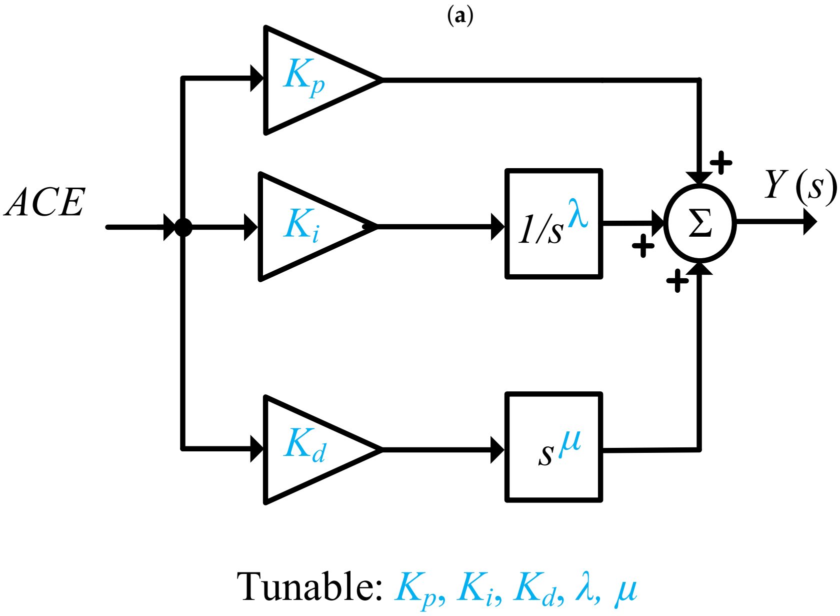

(**b**)

Figure 4. FOC-based LFCs block diagrams with tunable parameters. (**a**) TID control; (**b**) FOPID control.

A simplified version of the FOC-based LFC has been provided using TID control. The inclusion of a tilt term offers a simpler tuning process while enhancing the disturbance rejection effectiveness and improving robustness against existing uncertainties. The FOC-based TID is expressed as follows:

$$C_{TID}(s) = \frac{Y(s)}{E(s)} = K_t\, s^{-(\frac{1}{n})} + \frac{K_i}{s} + K_d\, s \tag{31}$$

where n is an FO tilt component's operator. Some additional hybrid FOC methods have been provided in the literature as follows:

$$C_{FOTID}(s) = \frac{Y(s)}{E(s)} = K_t\, s^{-(\frac{1}{n})} + \frac{K_i}{s^{\lambda}} + K_d\, s^{\mu} \tag{32}$$

$$C_{mFOTID}(s) = \frac{Y(s)}{E(s)} = K_p + K_t\, s^{-\left(\frac{1}{n}\right)} + \frac{K_i}{s^{\lambda}} + K_d\, s^{\mu} \tag{33}$$

3.2. FOC-Based LFC Representation

Compared with the IOC-based LFC, FOC-based LFC methods require special implementation procedures for FO operators representation. The value of the operator defines the control type. In general, FO operators defined by $D^{\alpha}|_a^t$ are classified as [61]:

$$D^{\alpha}|_a^t = \begin{cases} \alpha > 0 \;\rightarrow\; \frac{d^{\alpha}}{dt^{\alpha}} & \text{FO derivative} \\ \alpha < 0 \;\rightarrow\; \int_{t_0}^{t_f} dt^{\alpha} & \text{FO integral} \\ \alpha = 0 \;\rightarrow\; 1 & \end{cases} \tag{34}$$

The representation of FO operators is expressed using Riemann–Liouville, Grunwald–Letnikov, and Caputo fractional derivatives. In Grunwald–Letnikov, α_{th} is defined using the fractional derivative for f from limits a to t as [62]:

$$D^{\alpha}|_a^t = \lim_{h \to 0} \frac{1}{h^{\alpha}} \sum_{r=0}^{\frac{t-a}{h}} (-1)^r \binom{n}{r} f(t - rh) \tag{35}$$

where h stands for the sampling time, $[\cdot]$ is an integer operator, and n satisfies ($n - 1 < \alpha < n$). The binomial coefficients are defined as [62]:

$$\binom{n}{r} = \frac{\Gamma(n+1)}{\Gamma(r+1)\Gamma(n-r+1)'} \tag{36}$$

where gamma in (36) is a function expressed as [61]:

$$\Gamma(n+1) = \int_0^{\infty} t^{x-1} e^{-t}\, dt \tag{37}$$

Furthermore, use of the Riemann–Liouville approach eliminates the use of sums, and limits through using integer order derivatives, and integrals as in [63]:

$$D^{\alpha}|_a^t = \frac{1}{\Gamma(n-\alpha)} \left(\frac{d}{dt}\right)^n \int_a^t \frac{f(\tau)}{(t-\tau)^{\alpha-n+1}}\, d\tau \tag{38}$$

In Caputo representation, the definition is represented as [62]:

$$D^{\alpha}|_a^t = \frac{1}{\Gamma(n-\alpha)} \int_a^t \frac{f^{(n)}(\tau)}{(t-\tau)^{\alpha-n+1}}\, d\tau \tag{39}$$

Digital microcontroller representations are also crucial for FOC-based LFCs, of which, Oustaloup recursive-approximations (ORA) have shown proper implementable representation of FOC methods [61]. Their salient feature is suitability for digital signal processing unit implementations. The ORA definition is used in the paper for FOC implementation. The αth derivative operator (s^{α}) is defined mathematically as [61]:

$$s^{\alpha} \approx \omega_h^{\alpha} \prod_{k=-N}^{N} \frac{s + \omega_k^z}{s + \omega_k^p} \tag{40}$$

where ω_k^p and ω_k^z are defined as pole/zero locations, respectively, in ω_h sequence. They are determined using

$$\omega_k^z = \omega_b \left(\frac{\omega_h}{\omega_b}\right)^{\frac{k+N+\frac{1-\alpha}{2}}{2N+1}} \tag{41}$$

$$\omega_k^p = \omega_b \left(\frac{\omega_h}{\omega_b}\right)^{\frac{k+N+\frac{1+\alpha}{2}}{2N+1}} \tag{42}$$

$$\omega_h^\alpha = \left(\frac{\omega_h}{\omega_b}\right)^{\frac{-\alpha}{2}} \prod_{k=-N}^{N} \frac{\omega_k^p}{\omega_k^z} \tag{43}$$

The ORA approximated representation for FOC-based LFC possesses $(2N+1)$ poles/zeros, with N-order representation. The ORA representations for FOC LFCs in the paper are based on using N = 5 and the boundaries for the frequency are ($\omega \in [\omega_\mathrm{b}, \omega_\mathrm{h}]$) as $[10^{-3}, 10^3]$ rad/s.

3.3. Proposed FOC-Based LFC Using TFOID-Accelerated Controller

As clarified in the literature, PID, PIDA, TID, and FOPID represent the common LFC schemes in the literature. The proposed FOC-based LFC scheme is developed using hybridization of TID, PIDA, and FOPID controllers for LFC and EVs control. Figure 5 shows the proposed FOC-based LFC using the TFOID-Accelerated controller. It shares a tilt term as in TID with using two FO I, and D terms in addition to the accelerated term. From the FOPID side, the proposed TFOID-Accelerated shares FO I, and D terms with inclusion of tilt and accelerated terms. Also, it uses FO terms compared to IOC using the PIDA method. The inclusion of different FO terms leads to having much more design flexibility and better optimized design. In addition, it provides more tunable control parameters, which can enhance control performance with proper design optimization.

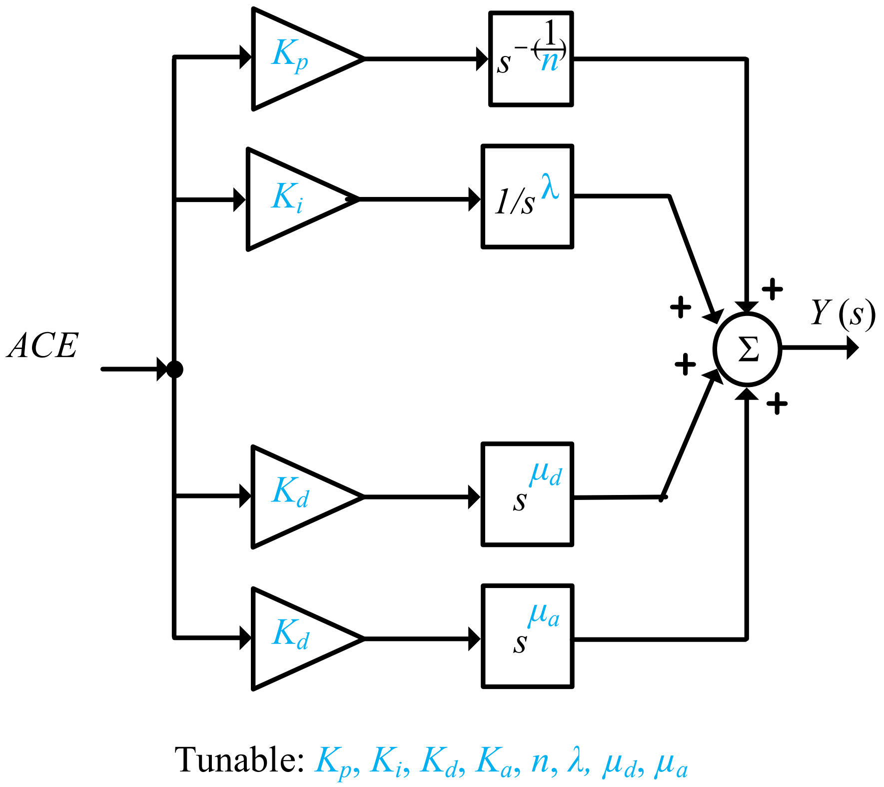

Figure 5. Structure of proposed TFOID-Accelerated with tunable parameters.

Therefore, a modified structure using TFOID-Accelerated control is proposed in the paper, merging characteristics of the PIDA, TID, and FOPID control schemes. The inclusion of the FO-based derivative, integrator, and accelerated terms leads to enhancing the closed loop system's stability and robustness. In addition, they provide the benefits of settling time reduction during disturbances. Thence, the TID control performance is enhanced with the added three terms in the proposed TFOID-Accelerated controller. It is also enriched with the added degree of freedom compared with the IOC-based derivative and integrator terms.

Therefore, a modified FOC-based LFC scheme is presented in this paper to enhance the performance of RES highly penetrated grids with V2G functionality. The proposed TFOID-Accelerated method is mathematically expressed as:

$$C(s) = \frac{Y(s)}{E(s)} = K_t\, s^{-\left(\frac{1}{n}\right)} + K_i \frac{1}{s^{\lambda}} + K_d\, s^{\mu_d} + K_a\, s^{\mu_a} \tag{44}$$

where K_t, K_i, K_d, and K_a are the tunable tilt, integrator, derivative, and accelerated gain terms. n, λ, μ_d, and μ_a are the tunable FO-based operators for the tilt, integrator, derivative, and accelerated terms. Figure 5 presents a block diagram model for the proposed TFOID-Accelerated controller.

From Figure 5, the proposed TFOID-Accelerated controller contains eight tunable controller parameters compared with three in IOC PIS, five in FOPID, four in TID, and four in the PIDA controller. By having the GO powerful metaheuristic algorithm in designing the controller, frequency regulation can be enhanced to a wide extent. The GO algorithm works through simultaneous tuning and determination of the eight parameters in each studied area, which leads to having an optimized vector of the control parameters together. Thence, the joint modified controller and the GO algorithm work together to provide better LFC performance.

4. Proposed Optimal Controller Design

4.1. Growth Optimizer Description and Algorithm

Recently the GO algorithm was presented in [64] and demonstrated superior performance in different optimization problems [65,66]. It emulates the learning process of individuals and the reflection mechanism on their growth in society. It involves two principal stages, including the learning stage and the reflection stage. Firstly, the learning stage involves the use of knowledge of individuals about other people's behavior differences in practice. Secondly, the reflection stage involves the use of different techniques for the identification and correction of existing shortcomings during the learning process [64]. In the GO algorithm, solutions for defined problems are represented by individuals [64], and the representation of decision variables is made through the individuals' necessary elements, such as emotions, beliefs, perseverance, morality, cultivation, etc. The main pseudo-code for the GO algorithm is shown in Algorithm 1 and is described in the remaining subsection.

Algorithm 1 Pseudo-code for proposed parameters tuning based on GO algorithm

```
Set GO algorithm parameters N, P1 = 5, P2 = 0.001, P2 = 3, and D
Set maximum iterations Max_FE settings N, P1 = 5, P2 = 0.001, P2 = 3, and D
Set tunable parameter limits (U, L) as L = (f)^min and U = (f)^max in (57) and (58)
Calculate initial population X_i as in (45)
while FE_s = 1 : Max_FE do
    for i = 1:N do                                                ▷ Learning Stage:
        Calculate worst and best solutions
    end for
    Calculate G1, G2, G3, G4, using (46)
    Calculate LF_k, where k = 1, 2, 3, 4 using (47)
    Calculate SF_i using (48)
    Calculate KA_s, where k = 1, 2, 3, 4 using (49)
    Continue the learning stage for ith individuals using (50) and its update in (51)
    for i = 1:N do                                                ▷ Reflection Stage:
        Complete the reflection phase for ith individuals as in (52), (53) and (54)
    end for
    Update ith individuals using (51)
    Update in real-time of best solution
end while
Return best parameters vectors                                    ▷ Sixteen parameters
```

A society of a certain number of individuals in a population is defined by a decision variable set as a matrix. For the ith individual and $i \in \{1, 2, 3, \ldots, N\}$, within the searching space $x_i \in \{x_{i,1}, x_{i,2}, \ldots, x_{i,D}\}$, where $x_{i,D}$ represents the Dth element for the ith individual. Moreover, the growth resistance GR defines the individual growth speed in the algorithm. The objective function for the desired optimization process takes the ith individual and returns the corresponding output GR_i for each ith individual. Having a lower growing GR by the individual means that it can absorb more knowledge. Therefore, it has a high possibility to be an elite member of society. In the algorithm, the population x_i, which represents the problem solution, is generated using [64]:

$$X_i = r \times (U - L) + L, \qquad i = 1, 2, \ldots, N \tag{45}$$

where r has a random value, and U and L represent the searching domain's limits for a desired optimization problem. Also, N represents the total solution number in x_i. In the GO method, x_i is divided into three parts according to the setting parameter P_1, wherein $P_1 = 5$, as defined in [64]. In the first part, the leader and elite members are set between 2 and P_1. In the second part, middle levels between $P_1 + 1$ and $N - P_1$ are involved. In the bottom level, the range between $N - P_1 + 1$ and N are included. The upper level's leader represents the best solution vector among the existing individuals in the GO method.

4.1.1. Learning Stage

Individual progress is enhanced to a great extent through the disparities confronting existing individuals. The main causes that lead to having differences and the learning processes derived from them are examined. In the GO method, learning stages simulate four main gaps that are defined as [65]:

$$\begin{aligned} G_1 &= X_b - X_{bt} \\ G_2 &= X_b - X_w \\ G_3 &= X_{bt} - X_w \\ G_4 &= X_{r1} - X_{r2} \end{aligned} \tag{46}$$

where X_b, X_{bt}, and X_w denote the best, the better, and the worst solution, respectively. Moreover, X_{r1} and X_{r2} are random solutions. G_k (in which $k \in \{1, 2, 3, 4\}$) are employed as a gap for improving learned skills and for decreasing knowledge differences. Also, the learning factor LF is employed for representing the parameter of reflecting the groups' variations. LF is defined as [66]:

$$LF_k = \frac{||G_k||}{\sum_{k=1}^{4} ||G_k||} \tag{47}$$

According to [64], each individual assesses his learned knowledge using SF_i, which is defined as [64]:

$$SF_i = \frac{GR_i}{GR_{max}} \tag{48}$$

where GR_{max} and GR_i denote the maximum GR for X and the individuals' growth X_i, respectively. Using the collected information in LF_k and SF_i, new knowledge is received for each X_i from each gap solution G_k using the knowledge acquisition KA_k. Based on [65], KA_k is defined as:

$$KA_k = SF_i \times LF_k \times G_k \qquad , \ k = 1, 2, 3, 4 \tag{49}$$

Solution X_i can improve its gained information through the following formulation [66]:

$$X_i(t+1) = X_i(t) + \sum_{k=1}^{4} KA_k \tag{50}$$

The quality of the updated values of X_i is estimated and compared with its last value to define whether there are significant differences or not. The $X_i(t+1)$ value is determined using [65]:

$$X_i(t+1) = \begin{cases} X_i(t+1) & \text{if } f_i^{t+1} < f_i^t \\ \begin{cases} X_i(t+1) & \text{if } r_1 < P_2 \text{ and} \\ & ind(i) = ind(1) \\ X_i(t) & else \end{cases} & Otherwise \end{cases} \tag{51}$$

where r_1 denotes a random number, and P_2 denotes the probability retention (with $P_2 = 0.001$). $ind(i)$ is the ranking of X_i in an ascending order based on the fitness value.

4.1.2. Reflection Stage

In this stage, individual persons need to learn how to reflect the knowledge, and individual persons need to check and identify their areas of weakness. Moreover, systematic learning procedures are used to understand their particular issues without providing solutions. They need to learn to repair bad issues through their individual actions. Furthermore, they have to retain and continue to gain good aspects. Thence, the reflective process can be mathematically defined as [64]:

$$X_i(t+1) = \begin{cases} X_m(t) & \text{if } r_2 < P_3 \\ X_i(t) & Otherwise \end{cases} \tag{52}$$

where $X_m(t)$ is represented as follows [66]:

$$X_m(t) = \begin{cases} r_4 \times (U - L) & \text{if } r_3 < AF \\ X_i(t) + r_5 \times (X_R - X_i(t)) & else \end{cases} \tag{53}$$

$$AF = 0.01 + 0.99 \times (1 - \frac{FE_s}{mac_{FE}}) \tag{54}$$

where r_3, r_4, and r_5 denote random variable values. X_R denotes the defined solution of the top $P_1 + 1$ solutions in X. AF denotes an attenuation factor that relies on the evaluation of FE and the total evaluations max_{FE}. After finishing the reflection stage, X_i should determine its growth rate as in the learning stage. Therefore, (51) is utilized for achieving the evaluation phase.

4.2. Proposed GO Algorithm-Based TFOID-Accelerated Design

The GO algorithm has been proven to perform better than others in different engineering problems. Optimizing control parameters using metaheuristic algorithms provides a way of determining optimum control parameters to achieve a specified objective. For tunable parameters, the proposed TFOID-Accelerated design has eight possible parameters to tune in each area. For area a in the studied system, the tunable parameters include K_{t1}, K_{i1}, K_{d1}, K_{a1}, n_1, λ_1, μ_{d1}, and μ_{a1}. In the same way, area b in the studied system has K_{t2}, K_{i2}, K_{d2}, K_{a2}, n_2, λ_2, μ_{d2}, and μ_{a2} as tunable parameters.

Accordingly, we have sixteen possible design optimization parameters as tunable using the GO algorithm. A new application of the GO algorithm is used to determine the best sixteen parameters set in a simultaneous tuning process for obtaining the best system response and rejecting existing disturbances. Usually, error functions are used for measuring frequency deviations, and the tie-line power is utilized for constructing the desired objective functions. Also, error functions are utilized to compare and determine the quality of the designed control systems. The primary error metrics consist of the integral squared error function (ISE), the integral absolute error function (IAE), the integral time-squared error function (ITSE), and the integral time-absolute error function (ITAE). The general mathematical expressions for these are as follows:

$$
\begin{aligned}
ISE &= \int \sum_{i=1}^{m} (e_i^2)\, \mathrm{d}t \\
IAE &= \int \sum_{i=1}^{m} abs(e_i)\, \mathrm{d}t \\
ITSE &= \int \sum_{i=1}^{m} (e_i^2)\, t.\mathrm{d}t \\
ITAE &= \int \sum_{i=1}^{m} abs(e_i)\, t.\mathrm{d}t
\end{aligned}
\tag{55}
$$

For the studied system, the minimization objective function is designed for reducing frequency deviations in both areas Δf_a and Δf_b in addition to reducing the deviations in the tie-line power ΔP_{tie} between areas. As a result, three elements are used for constructing the desired design objectives of the studied system, including Δf_a, Δf_b, and (ΔP_{tie}). Equal weightings are given for the three measurements in forming the error functions. Thence, the IAE, ISE, ITAE, and ITSE error functions in (55) are formed as:

$$
\begin{aligned}
IAE &= \int_0^{t_s} (abs(\Delta f_a) + abs(\Delta f_b) + abs(\Delta P_{tie}))\, \mathrm{d}t \\
ISE &= \int_0^{t_s} ((\Delta f_a)^2 + (\Delta f_b)^2 + (\Delta P_{tie})^2)\, \mathrm{d}t \\
ITAE &= \int_0^{t_s} (abs(\Delta f_a) + abs(\Delta f_b) + abs(\Delta P_{tie}))\, t.\mathrm{d}t \\
ITSE &= \int_0^{t_s} ((\Delta f_a)^2 + (\Delta f_b)^2 + (\Delta P_{tie})^2)\, t.\mathrm{d}t
\end{aligned}
\tag{56}
$$

In each iteration, a set of values for the sixteen tunable parameters is determined by the GO algorithm, in which the values are constrained by the boundaries defined as:

$$
\begin{aligned}
K_t^{min} &\le K_{t1}, K_{t2} \le K_t^{max} \\
K_i^{min} &\le K_{i1}, K_{i2} \le K_i^{max} \\
K_d^{min} &\le K_{d1}, K_{d2} \le K_d^{max} \\
K_a^{min} &\le K_{a1}, K_{a2} \le K_a^{max} \\
n^{min} &\le n_1, n_2 \le n^{max} \\
\lambda^{min} &\le \lambda_1, \lambda_2 \le \lambda^{max} \\
\mu_d^{min} &\le \mu_{d1}, mu_{d2} \le mu_d^{max} \\
\mu_a^{min} &\le \mu_{a1}, mu_{a2} \le mu_a^{max}
\end{aligned}
\tag{57}
$$

where $(f)^{max}$ and $(f)^{min}$ are the constraining upper and lower limits for each of the tunable sixteen parameters. The values of $(f)^{max}$ and $(f)^{min}$ are used in the proposed method as follows:

$$
\begin{gathered}
0 \leq K_{t1}, K_{t2} \leq 5 \\
0 \leq K_{i1}, K_{i2} \leq 5 \\
0 \leq K_{d1}, K_{d2} \leq 5 \\
0 \leq K_{a1}, K_{a2} \leq 5 \\
2 \leq n_1, n_2 \leq 10 \\
0 \leq \lambda_1, \lambda_2 \leq 1 \\
0 \leq \mu_{d1}, \mu_{d2} \leq 1 \\
1 \leq \mu_{a1}, \mu_{a2} \leq 2
\end{gathered} \tag{58}
$$

The constraints in (58) are employed in the GO algorithm parameter searching process. A complete diagram of the optimization procedure is shown in Figure 6 for the proposed GO algorithm-based TFOID-Accelerated method. The modeled case study of the two-area MG system is implemented in Matlab Simulink. At the same time, the modeled MG system is linked with the m-file code in the Matlab environment, which includes the GO algorithm with the defined parameter bounds and algorithm settings. The GO algorithm is responsible for the searching process and outputting the best parameter values for the designed controllers. The guiding of the searching process uses the objective function, which is defined in (55) for the current optimization problem, and the boundary constraints for the parameters are defined in (57) and (58). The three variables (Δf_a, Δf_b, and ΔP_{tie}) measured in the Simulink model are fed into the GO m-file algorithm during the defined number of runs. Afterward, the calculated objective is compared with the stored global optimum one, which is updated when the current one has a better value. Finally, if the maximum iteration number reaches the stopping criteria, the obtained optimum parameter values are output in addition to their associated convergence curve of the algorithm evaluations. The outputs include the best parameter set that is employed for the results and comparison of the designed and proposed control method. Table 3 shows the obtained controller parameter in the optimization process.

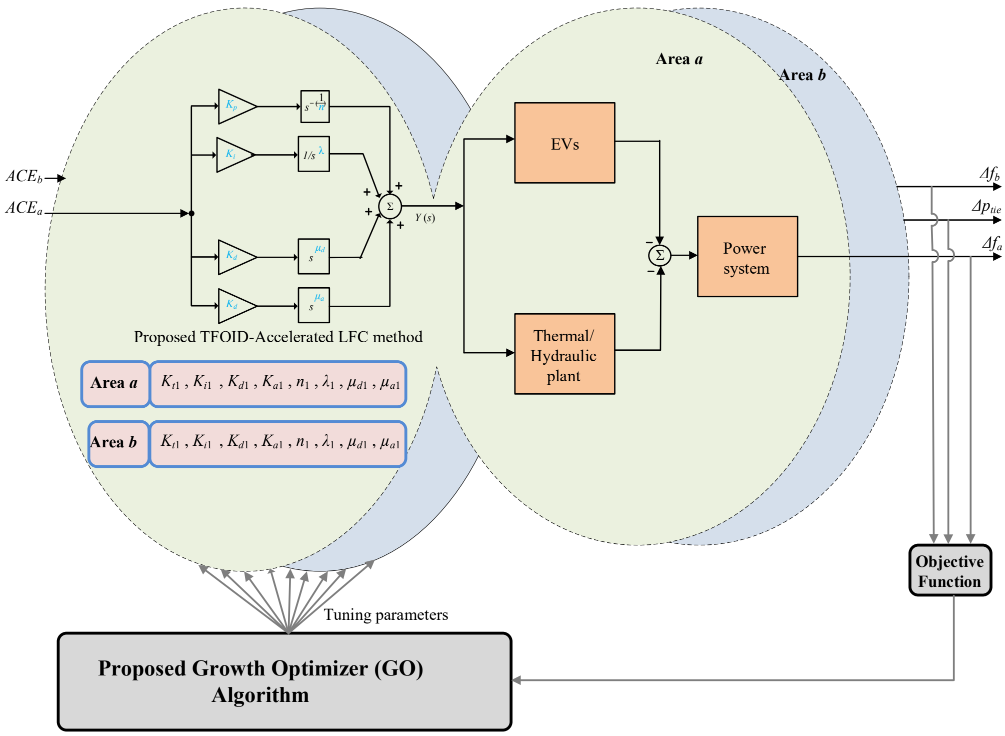

Figure 6. Overall optimization structure of proposed TFOID-Accelerated based on the GO algorithm.

Table 3. Controller parameters for different areas.

Controller	Area	K_p	K_i	K_d	K_t	K_a	n	λ	μ_1	μ_2
PID	Area-*a*	4.9765	4.8871	4.3139	—	—	—	—	—	—
	Area-*b*	4.3636	3.4465	1.2884	—	—	—	—	—	—
PID-Accelerated	Area-*a*	3.0992	3.9542	1.0558	—	2.0205	—	—	—	1.556
	Area-*b*	3.9701	2.9021	1.9667	—	1.3563	—	—	—	1.238
TID	Area-a	—	2.5674	3.9984	1.8184	—	4.955	—	—	—
	Area-*b*	—	1.1892	1.9497	2.9809	—	4.961	—	—	—
TFOID-Accelerated	Area-*a*	—	4.8906	4.7948	4.0327	2.3681	2.631	0.923	0.416	1.271
	Area-*b*	—	3.4132	3.2288	4.2643	2.1538	3.028	0.499	0.723	1.682

5. Results and Discussion

The MATLAB/SIMULINK package (version 2022b) is applied to establish a thermal and hydraulic generators two-area non-linear power system model for simulation verification of the proposed control method, as shown in Figure 2. This Simulink package is linked with the GO algorithm coding to optimally tune the parameters of the suggested controllers, such as PID, PID-A, TID, and the proposed TFOID-Accelerated controller to obtain the best performance from the conventional generators, RESs, and EVs. To evaluate this performance, several simulation tests were performed. The load dynamics and correlated uncertainties are the main sources of frequency instability. Therefore, the studied two-area system was tested with different shapes of load disturbances, such as, step load perturbation, two-step change and multi-load change, which are considered as the worst cases of load variation. Moreover, the intermittency of PV and wind generators were applied to the two-area system for examining the capability of the proposed control technique in enhancing the frequency regulation of the hybrid power system. Furthermore, the uncertainties of the turbine, governor, and generator time-constant were applied to demonstrate the robustness of the accelerated fractional-tilt controller. The GO algorithm was utilized in this work as it has faster and smoother convergence characteristics than other meta-heuristic algorithms, such as PSO, SCO, and WOA, as shown in Figure 7. The convergence process is run at 20 populations and a 100 maximum iterations number on a personal computer with an Intel Core i7 CPU of 2.6 GHz and 64-bit processor. The simulation results are organized as follows:

- **Scenario 1:** The impact of one-step load pattern (1SLP).
- **Scenario 2:** The impact of two-step load pattern (2SLP).
- **Scenario 3:** The impact of multi-load pattern (MLP).
- **Scenario 4:** The impact of the RESs fluctuations.
- **Scenario 5:** The impact of high penetration of RESs fluctuations.
- **Scenario 6:** The impact of parameters uncertainties.

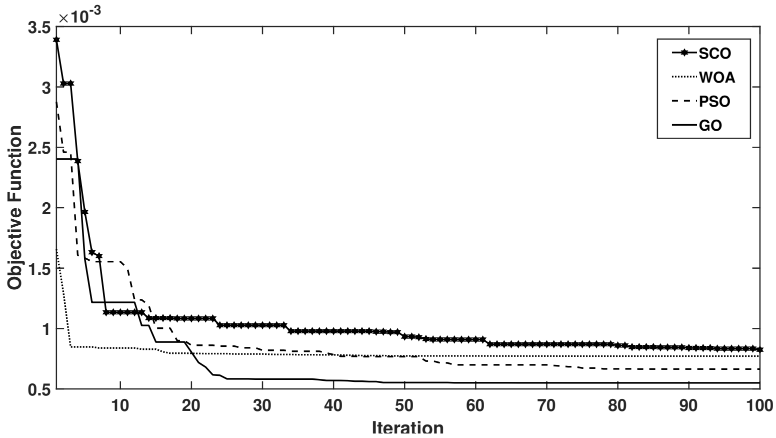

Figure 7. Convergence curve of GO algorithm against other techniques.

5.1. Scenario 1

This investigation contrasts the performance of the TFOID-Accelerated controller with that of traditional PID, PIDA, and TID control techniques in a dual-area microgrid system. A one-step load perturbation (1SLP) of 1% is introduced in region-1 at the beginning of the simulation to evaluate each controller's effectiveness. The optimization approach, based on GO, effectively mitigates fluctuations in frequency deviation across region-1 (Δf_1), region-2 (Δf_2), and the interconnected tie-line power (ΔP_{tie}), as illustrated in Figure 8a–c. The results indicate that the TFOID-Accelerated controller achieves the lowest peak undershoot, with values of 0.0014 Hz in region-1 and 0.00092 Hz in region-2, alongside almost no overshoot and a tie-line peak power of 0.00035 p.u. Meanwhile, the TID controller manages to lower the peak undershoot to 0.0036 Hz and 0.0032 Hz in region-1 and region-2, respectively. On the other hand, the PIDA exhibits significant overshoots of 0.0049 Hz and 0.0034 Hz and longer settling times compared to the other controllers. Additionally, the standard PID controller shows the poorest performance with peak undershoots of 0.0054 Hz in region-1 and 0.0038 Hz in region-2, and a tie-line power deviation of about 0.0011 p.u., making it the least effective in this scenario. An in-depth comparison of these control methods regarding settling time (ST), overshoot (O_{sh}), and undershoot (U_{sh}) for frequency oscillations and tie-line power changes is presented in Table 4. Moreover, the superior performance of the TFOID-Accelerated controller is confirmed through the analysis of ISE, ITSE, IAE, and ITAE for the optimization scenarios depicted in Figure 9. These analyses reveal that the TFOID-Accelerated control structure achieves the most significant reduction in the objective functions across all metrics.

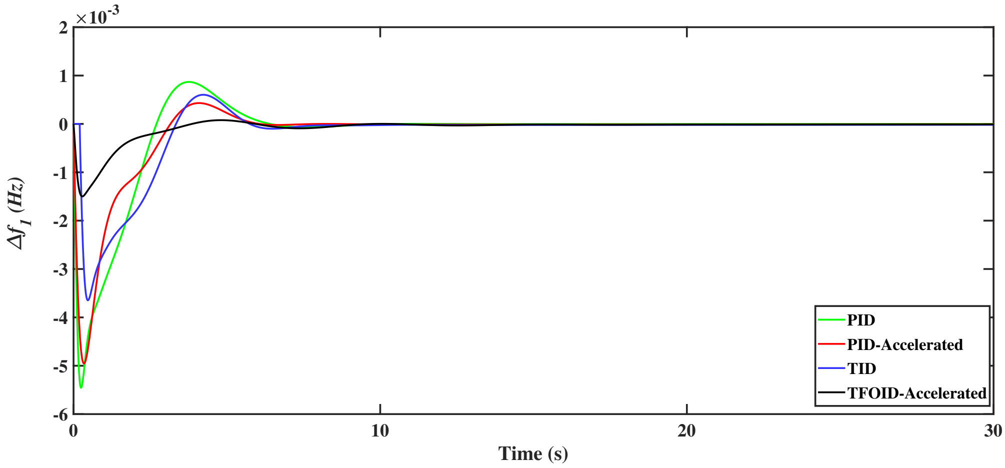

(**a**)

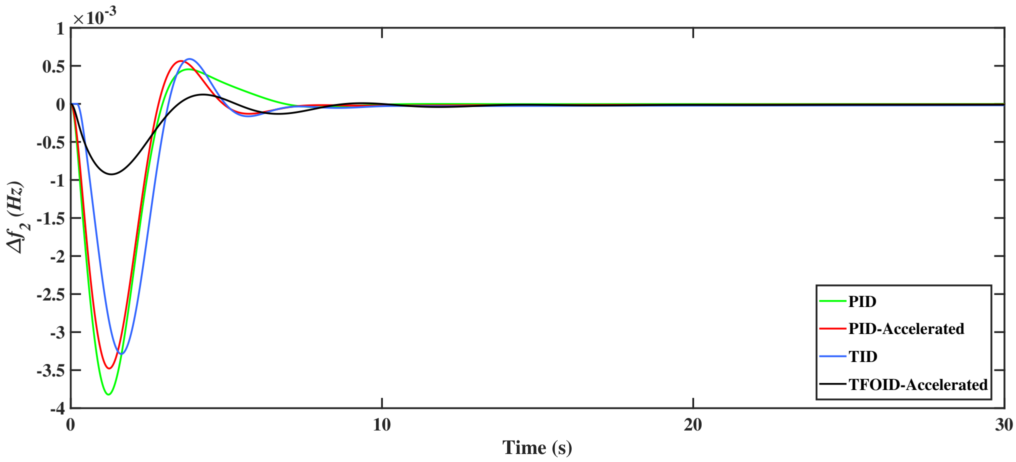

(**b**)

Figure 8. *Cont.*

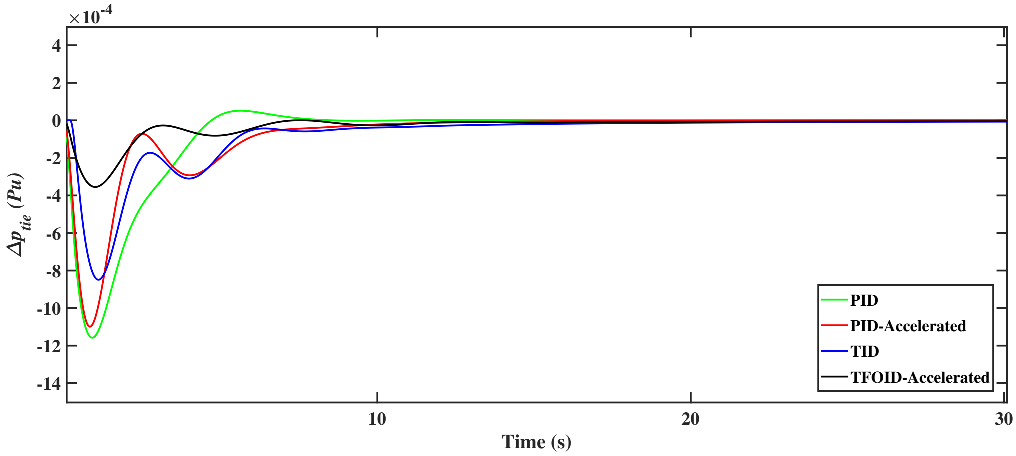

(c)

Figure 8. Frequency dynamic responses of Scenario 1. (**a**) Δf_a; (**b**) Δf_b; (**c**) ΔP_{tie}.

Table 4. Performance metrics; Osc. denotes oscillation.

		Δfa			Δfb			ΔP_{tie}		
		O_{sh}	U_{sh}	ST	O_{sh}	U_{sh}	ST	O_{sh}	U_{sh}	ST
CASE 1	PID	0.00086	0.0054	17.11	0.00051	0.0038	21.45	0.00005	0.0011	18.32
	TID	0.00043	0.0049	16.12	0.00055	0.0034	18.22	-	0.0010	16.89
	FOTID	0.00059	0.0036	14.12	0.00054	0.0032	15.14	-	0.00084	14.75
	TFOID-Accelerated	-	0.0014	10.42	0.00012	0.00092	13.02	-	0.00035	12.81
CASE 2 40 s	PID	0.0012	0.022	57.99	0.0066	0.036	56.43	0.0093	0.00048	>100 s
	TID	0.00056	0.016	50.13	0.00086	0.022	52.78	0.0061	0.00027	>100 s
	FOTID	-	0.014	38.65	0.0019	0.021	38.76	0.0.0056	-	>100 s
	TFOID-Accelerated	0.00038	0.0091	37.98	0.0018	0.011	37.96	0.0038	0.00019	49.01
CASE 3 30 s	PID	0.0045	0.027	51.76	0.0026	0.016	51.52	0.00028	0.0055	50.22
	TID	0.0025	0.021	49.53	0.0024	0.014	49.53	0.00012	0.0041	48.40
	FOTID	0.0023	0.013	45.78	0.0022	0.013	45.76	0.00009	0.0026	43.19
	TFOID-Accelerated	0.00023	0.0041	38.54	0.00041	0.0029	41.11	0.00002	0.0011	39.21
CASE 4 30 s	PID	0.022	0.0014	Osc.	0.036	0.0071	Osc.	0.00044	0.0095	Osc.
	TID	0.015	0.00079	Osc.	0.021	0.00086	Osc.	0.00028	0.0059	Osc.
	FOTID	0.0092	0.00019	Osc.	0.013	0.0016	Osc.	0.00017	0.0039	Osc.
	TFOID-Accelerated	0.0042	0.00024	Osc.	0.0053	0.00083	Osc.	0.00002	0.0019	Osc.
CASE 5	PID	0.03525	0.00445	Osc.	0.04935	0.00617	Osc.	0.00116	0.00532	Osc.
	TID	0.01913	-	Osc.	0.02931	0.00201	Osc.	0.00081	0.00469	Osc.
	FOTID	0.01464	-	Osc.	0.0218	0.00145	Osc.	0.00058	0.00221	Osc.
	TFOID-Accelerated	0.00521	-	Osc.	0.00788	0.00106	Osc.	0.00055	0.00158	Osc.

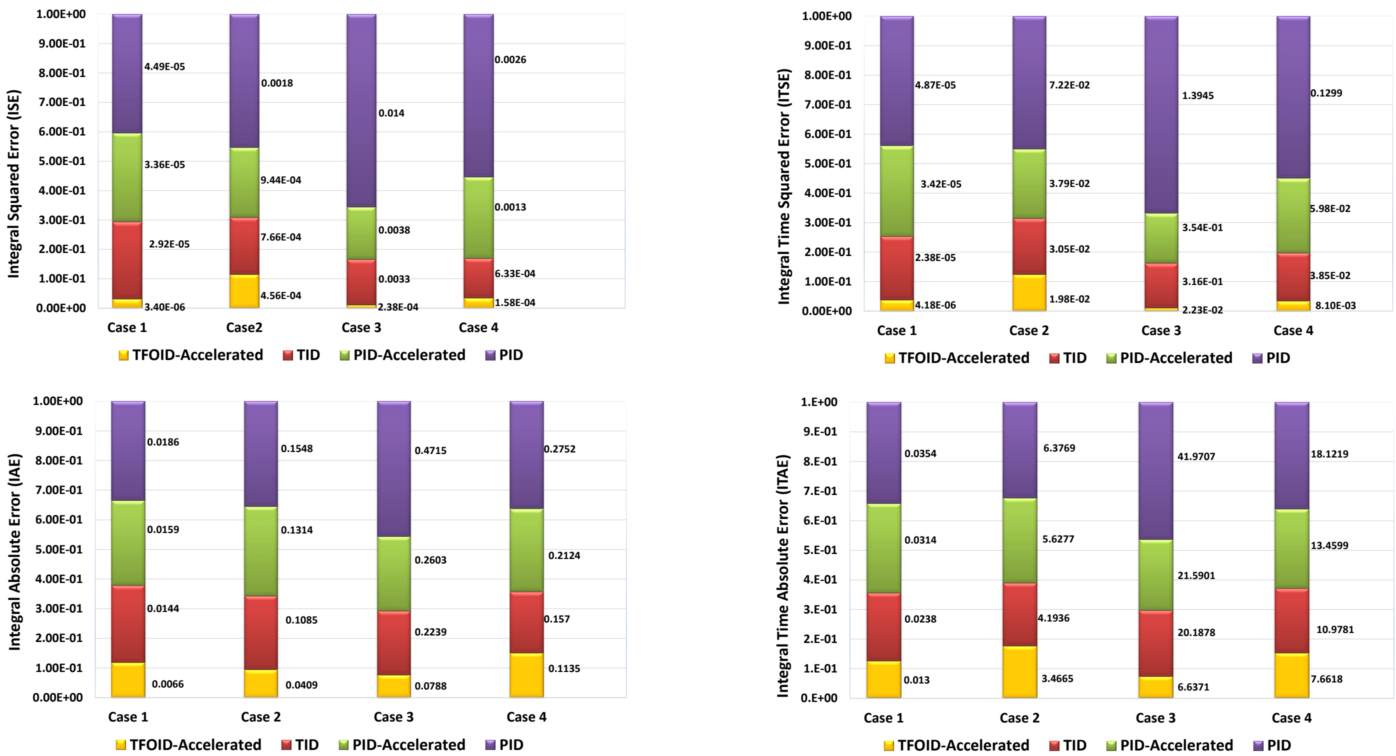

Figure 9. Objective functions comparison at Scenario 1.

5.2. Scenario 2

The primary aim of this scenario is to evaluate the efficacy of the TFOID-Accelerated controller in a dual-area MG system, particularly focusing on the integration of EVs utilizing the GO algorithm, against a backdrop of two-step load perturbations (2SLP) in region-1 at $t = 0$ s and region-2 at $t = 40$ s. The performance of the MG system under these conditions, including frequency deviations and tie-line power variations, is showcased in Figure 10, comparing the TFOID-Accelerated controller with other control methods such as PID, PIDA, TID, all optimized using the GO technique. The results illustrate that the TFOID-Accelerated controller outperforms its counterparts by significantly reducing frequency and power fluctuations, as evidenced by its settling times (37.98, 37.95, and 49.01) and undershoots (0.0091, 0.011, and 0.0038) for region-1, region-2, and the interconnecting line power, respectively, at 40 s. Following in effectiveness, the TID method reduces frequency and power instabilities to undershoots of (0.014, 0.021, and 0.0056) and settling times of (38.65, 38.78, and >100), respectively. The PIDA controller ranks third, stabilizing frequency and power deviations with values of (0.016, 0.022, and 0.0061) for undershoots and returning to a stable state within (50.31, 52.78, and >100) for settling times. Lastly, the PID controller demonstrates the longest settling times (57.99, 56.43, and >100) and highest undershoots (0.022, 0.036, and 0.0093) for region-1, region-2, and the interconnecting line power variation, respectively. These results highlight the superior performance of the TFOID-Accelerated controller with EV integration via the GO algorithm over the PID, PIDA, and TID controllers optimized by the same technique, in terms of overshoot (O_{sh}), undershoot (U_{sh}), and settling time (ST), as detailed in Table 4.

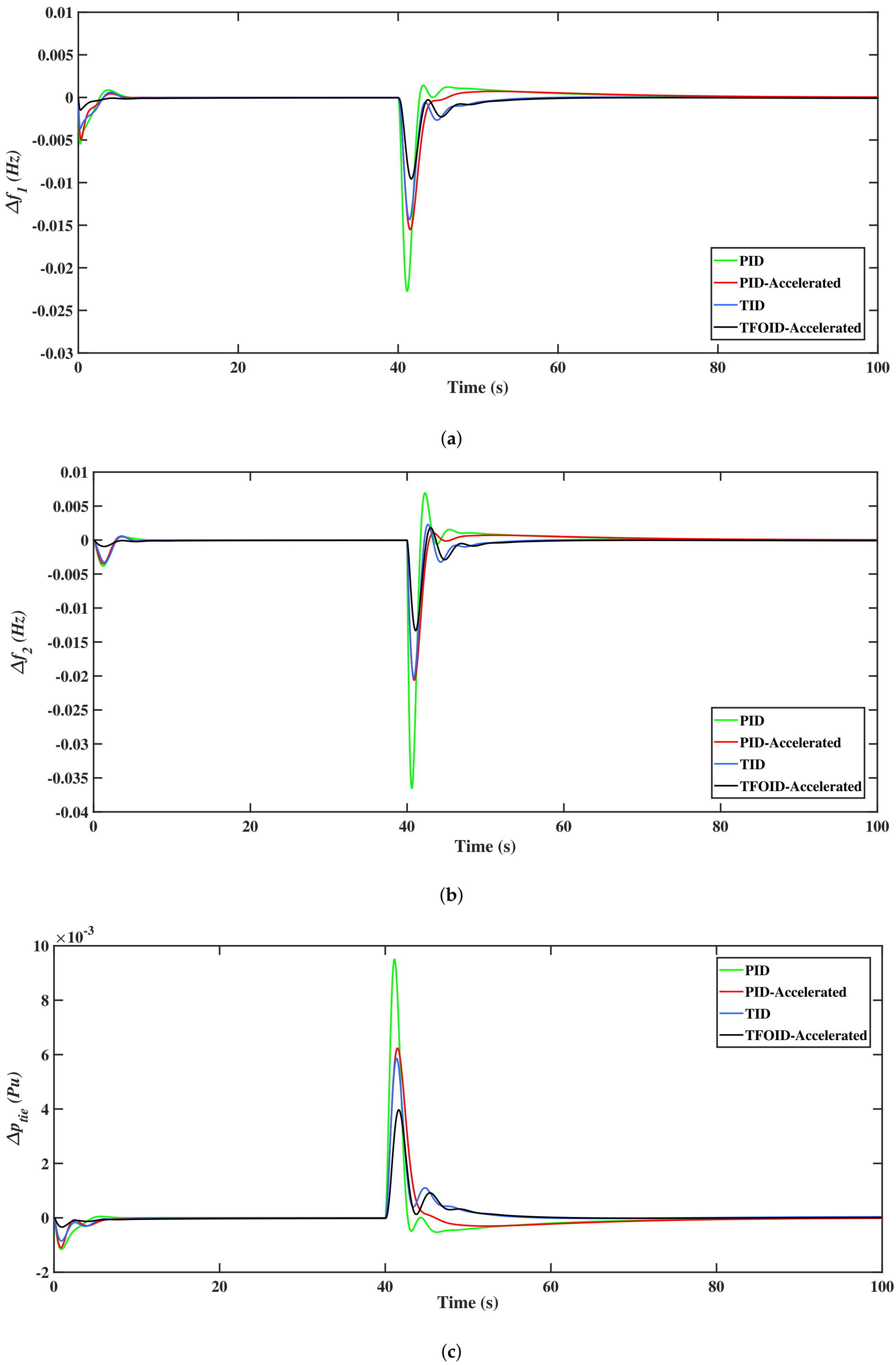

Figure 10. Frequency dynamic responses of Scenario 2. (**a**) Δf_a; (**b**) Δf_b; (**c**) ΔP_{tie}.

5.3. Scenario 3

In this scenario, the effectiveness of the TFOID-Accelerated controller as an LFC mechanism and the integration of controlled EVs through the GO algorithm are evaluated against a backdrop of significant multi-load variation patterns (MLVP) in region-1, as depicted in Figure 11. This scenario introduces MLVPs with a 10% increase at 30 s, a 15% increase at 70 s, and a 25% decrease at 110 s in the interconnected dual-area MG system. Each region incorporates an EV system contributing 10% of the system's rating to MG frequency stabilization. The robustness of the TFOID-Accelerated-based LFC is demonstrated by comparing it with traditional control schemes like PID, PIDA, and TID. Figure 12 presents the waveforms of the MG tie power and frequency deviations in response to MLVPs. The dynamic performance of the proposed TFOID-Accelerated/EV approach outperforms the alternatives by achieving quicker adjustments and minimal distortion. The results indicate that this approach effectively controls the frequency deviation, limiting it to −0.0041 Hz in region-1 and −0.0029 Hz in region-2 at 30 s, with smooth and consistent settling times. The TID controller, paired with EV systems, ranks next, offering frequency deviations of approximately −0.013 Hz in both regions and a −0.0026 p.u. deviation in tie-line power, as detailed in Table 4. The PIDA controller follows, managing to maintain the frequency at −0.021 Hz in region-1 and −0.014 Hz in region-2. The PID strategy, while capable of addressing system frequency and tie-line power deviations, results in longer settling times (ST) and greater oscillations in overshoot (O_{sh}) and undershoot (U_{sh}) beyond ±0.07 Hz, especially during periods of intense MLVP at 70 and 110 s. Thus, the analysis clearly demonstrates that the most effective performance stems from the synergy of TFOID-Accelerated/LFC and controlled EV charging/discharging systems, leveraging the GO algorithm for optimization.

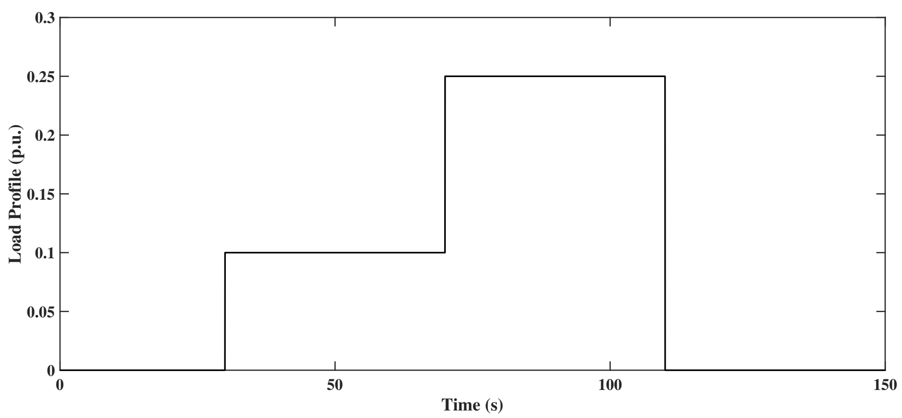

Figure 11. MLP profile for Scenario 3.

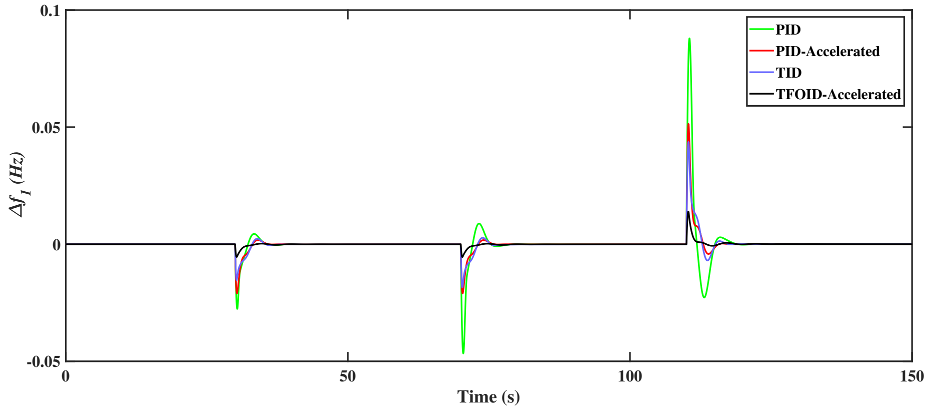

(**a**)

Figure 12. *Cont.*

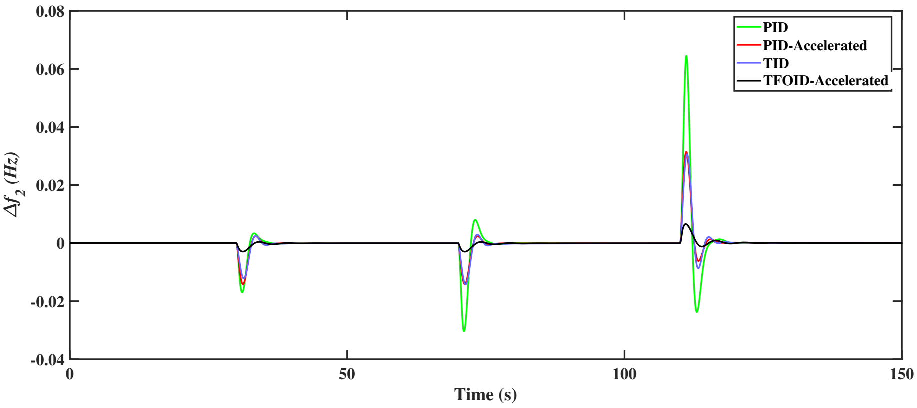

(**b**)

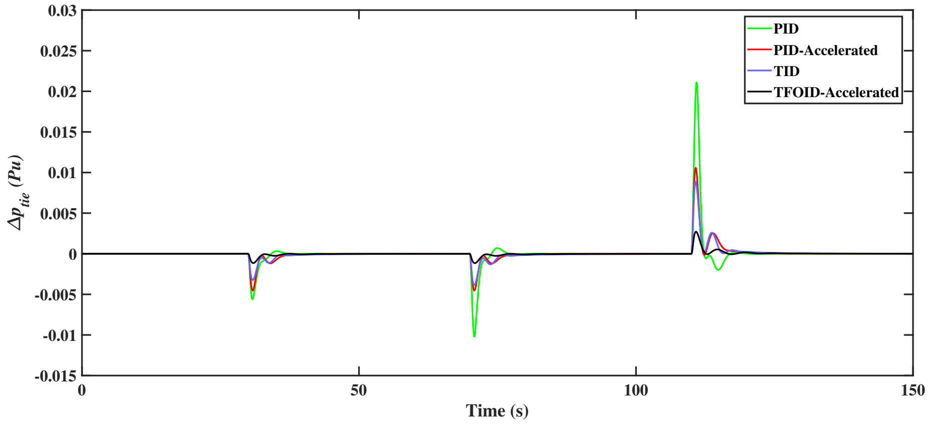

(**c**)

Figure 12. Frequency dynamic responses of Scenario 3. (**a**) Δf_a; (**b**) Δf_b; (**c**) ΔP_{tie}.

5.4. Scenario 4

This scenario assesses the resilience of the proposed TFOID-Accelerated LFC system, integrated with EV sharing via the GO algorithm, against severe fluctuations introduced by photovoltaic (PV) generation at 30 s and unpredictable wind speed changes at 100 s, in addition to a single load perturbation (SLP) at the simulation's onset. Consequently, the microgrid (MG) power system confronts significant challenges in maintaining frequency and tie-line power stability due to the intermittent nature of the renewable energy source (RES) inputs alongside load variations, as illustrated in Figure 13. The efficacy of various proposed LFC mechanisms in managing the frequency and tie-line power across the dual-area MG system is showcased in Figure 14. Observations from this figure reveal that with the PID controller, there is a notable frequency discrepancy during the integration phases of PV and wind energy, recording deviations of 0.022 Hz and 0.026 Hz for region-1, and 0.037 Hz and 0.015 Hz for region-2, respectively. The PID-Accelerated controller offers improved outcomes over the standard PID, with deviations of 0.015 Hz and 0.014 Hz in region-1 at 30 and 100 s, respectively, and 0.021 Hz and 0.011 Hz in region-2, albeit it struggles with extended damped oscillations, particularly during the initiation of PV power. The TID controller, while demonstrating marginally better frequency stability than PID and PID-Accelerated controllers, still suffers from prolonged recovery times to neutralize oscillations fully. In contrast, the TFOID-Accelerated controller excels in swiftly countering frequency and tie-line power fluctuations, achieving a lower steady-state error than both conventional and other accelerated controllers. This analysis underlines the TFOID-Accelerated controller's robustness, as optimized by the GO technique, in handling extreme conditions effectively. It significantly enhances the EV integration process, enabling rapid energy exchange with the MG system during critical moments of wind and PV connections. Thus, it demonstrates reliable performance irrespective of the disturbance's origin, whether from generation or load changes.

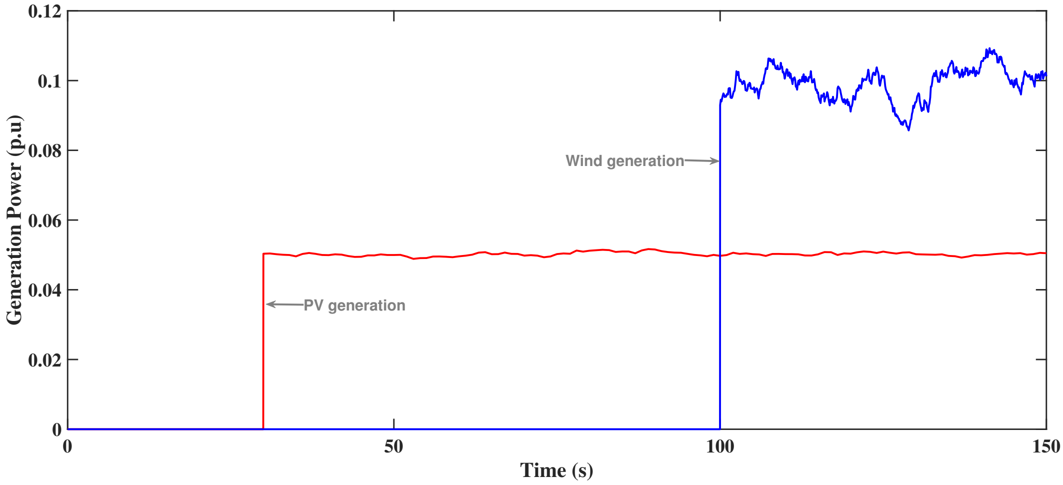

Figure 13. RESs profile for Scenario 4.

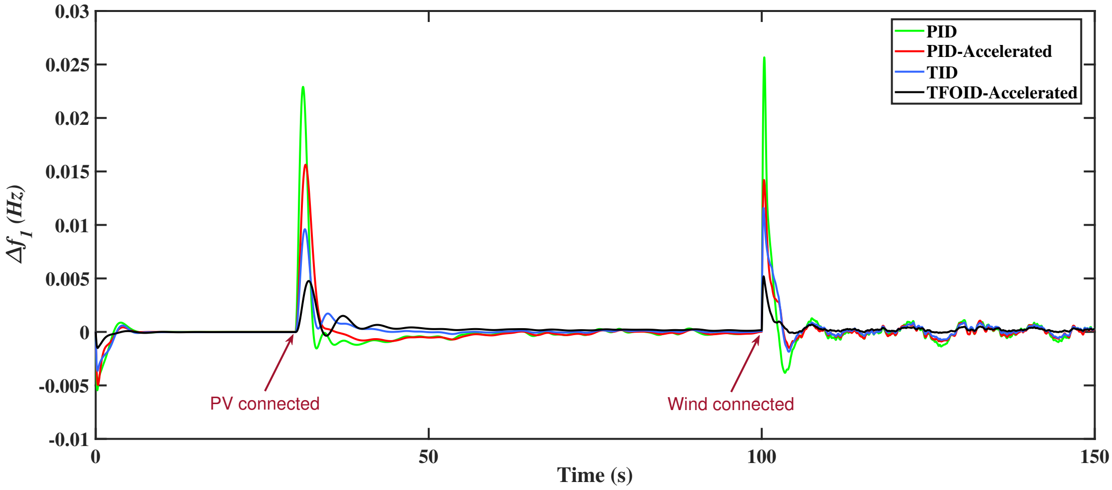

(**a**)

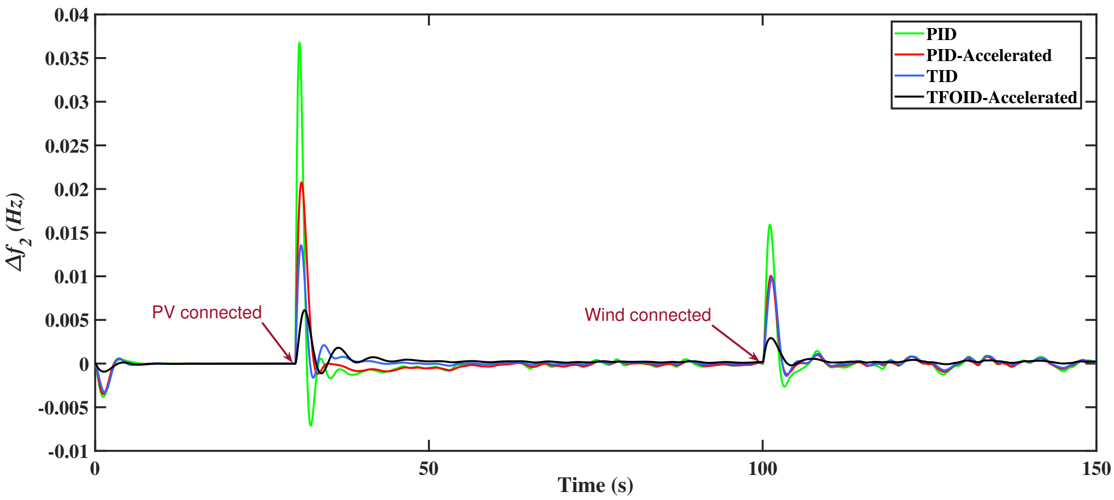

(**b**)

Figure 14. *Cont.*

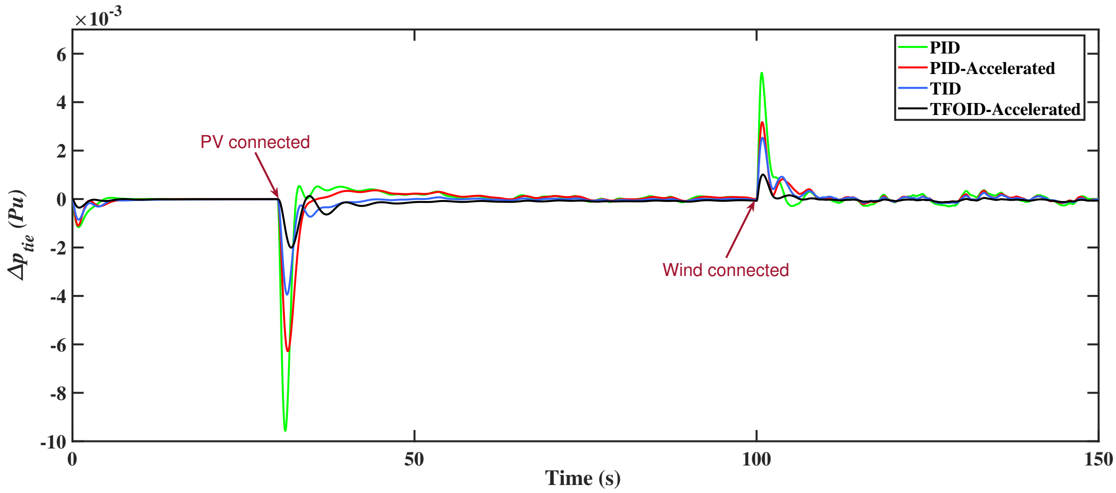

(**c**)

Figure 14. Frequency dynamic responses of Scenario 4. (**a**) Δf_a; (**b**) Δf_b; (**c**) ΔP_{tie}.

5.5. Scenario 5

This scenario provides additional evidence supporting the effectiveness of the newly proposed TFOID-Accelerated controller as an LFC and its impact on integrating EVs for frequency stabilization within a dual-area microgrid (MG). To this end, a scenario involving significant renewable energy sources (RESs) penetration is simulated from the onset, representing a critical test for the transient stability of the multi-area MG power system. Specifically, a 0.07 p.u photovoltaic (PV) unit is integrated into region-2, and a 0.12 p.u wind generation unit is introduced in region-1 at the initial second. Observations from Figure 15 indicate that the initial transient response of the MG system to the simultaneous introduction of PV and wind power, particularly under a conventional PID control scheme, leads to a temporary spike in frequency variations and tie-line power adjustments. These spikes exceed +0.035 Hz in region-1 and +0.05 Hz in region-2. In contrast, employing the PID-Accelerated control method mitigates these deviations to +0.016 Hz in region-1 and just over +0.02 Hz in region-2. Furthermore, the TID control strategy further reduces these deviations to +0.012 Hz in region-1 and slightly over +0.01 Hz in region-2. However, the most significant reduction in frequency and power deviations is achieved with the innovative TFOID-Accelerated controller. This controller not only outperforms the others in stabilizing frequency and power but also demonstrates a profound capability to enhance the EV integration process, effectively handling the challenges posed by the high RES penetration.

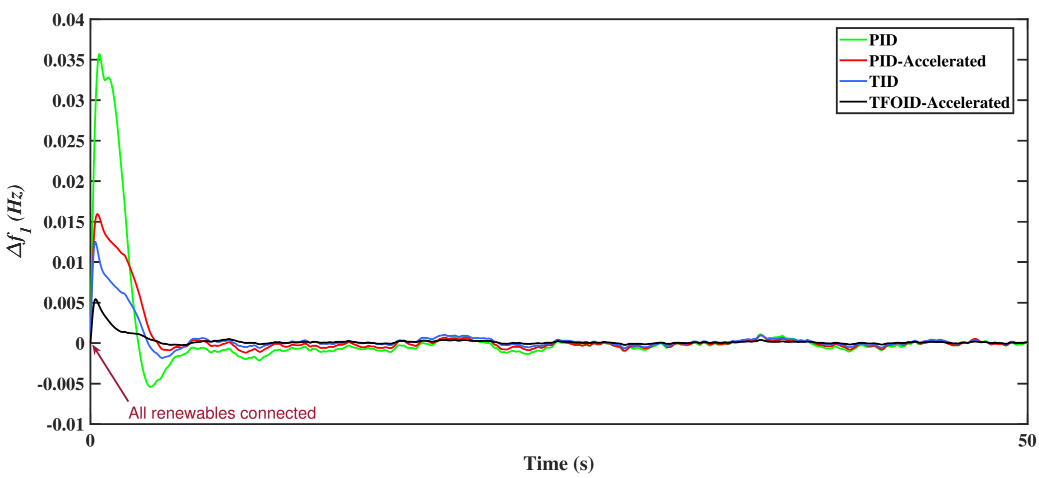

(**a**)

Figure 15. *Cont.*

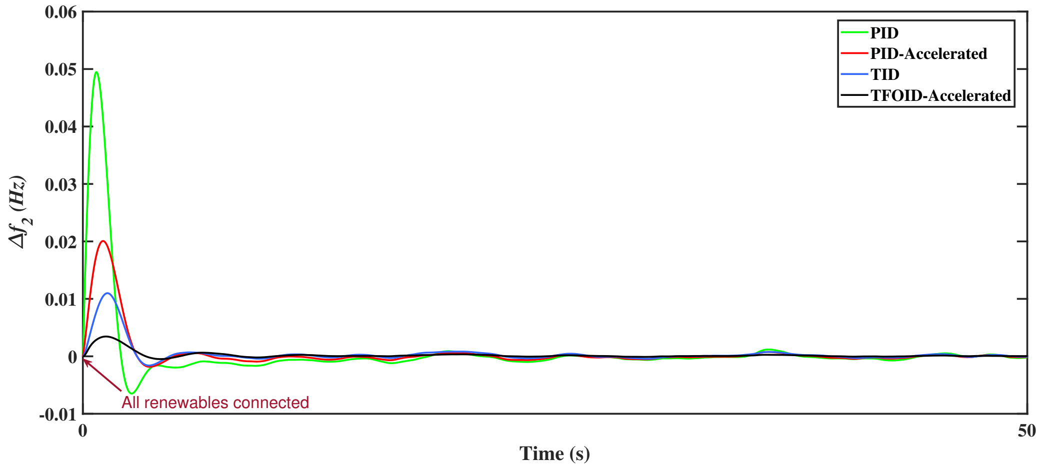

(**b**)

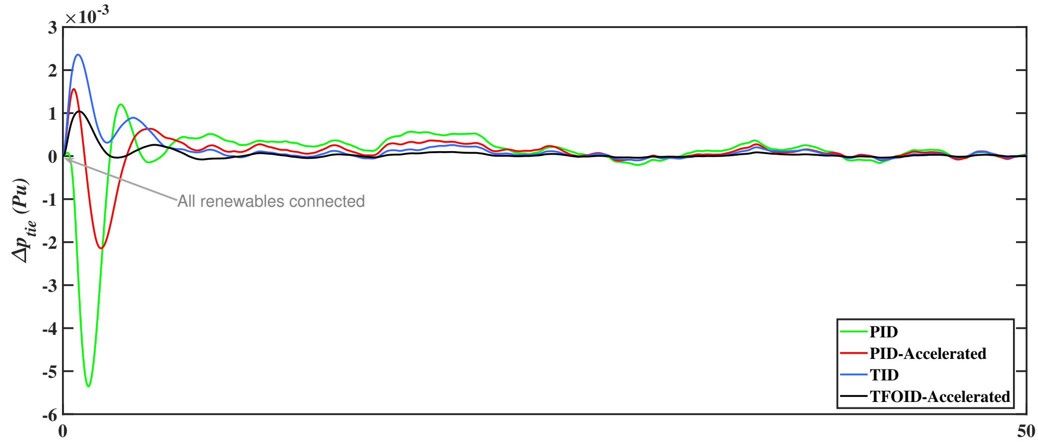

(**c**)

Figure 15. Frequency dynamic responses of Scenario 5. (**a**) Δf_a; (**b**) Δf_b; (**c**) ΔP_{tie}.

5.6. Scenario 6

Sudden load fluctuations and external influences can lead to adjustments in the control design requirements, highlighting the necessity of evaluating the TFOID-Accelerated controller's adaptability to parameter variations. This scenario demonstrates the impact of varying generation parameters (T_t, T_g, R, and β) by $\pm$50% on the frequency and tie-line power dynamics within the examined microgrid (MG) system. A comparative analysis of the proposed controller's efficiency against traditional PID, PIDA, and TID controllers under both standard operating conditions and scenarios with altered system parameters is conducted. The response of the dual-area MG power system, specifically frequency deviations (Δf_1, Δf_2) and the power in the interconnected region (ΔP_{tie}) managed by the proposed controller, is detailed in Table 5. This table reveals that modifications in the system parameters by $\pm$50% tend to exacerbate overshoot and undershoot phenomena. Nevertheless, it demonstrates the TFOID-Accelerated control strategy's superior stability and promptness in correcting frequency and tie-line power deviations more effectively and swiftly compared to traditional and other accelerated control methods.

Table 5. Sensitivity analysis results.

Parameter	Change	Controller	Δ_{f_a}			Δ_{f_b}			ΔP_{tie}		
			MO	MU	ST	MO	MU	ST	MO	MU	ST
T_t	+50%	PID	0.00096	0.00622	20.19	0.00074	0.00409	19.17	0.00004	0.00131	23.85
		TID	0.00068	0.00565	18.46	0.00066	0.00371	16.52	0.00001	0.00125	22.31
		FOTID	0.00051	0.00422	14.32	0.00078	0.0034	14.97	–	0.00095	18.53
		FOTIDA	0.00010	0.00179	12.12	0.00016	0.00097	14.48	–	0.00039	18.41
	−50%	PID	0.00063	0.00429	19.22	0.00039	0.00363	16.43	0.00003	0.00103	17.21
		TID	0.00020	0.00392	17.33	0.00016	0.00341	15.33	–	0.00096	15.66
		FOTID	0.00026	0.00276	15.23	0.00013	0.00322	13.79	–	0.00075	14.98
		FOTIDA	0.00003	0.00118	14.44	0.00005	0.00091	13.47	–	0.00032	14.53
T_g	+50%	PID	0.00078	0.0055	16.21	0.00048	0.00368	19.55	0.00003	0.00113	22.14
		TID	0.00036	0.0053	15.72	0.00048	0.00346	18.11	–	0.00114	20.22
		FOTID	0.00048	0.0040	13.99	0.00049	0.00322	15.90	–	0.00087	18.19
		FOTIDA	0.00007	0.0016	13.54	0.00011	0.00092	15.11	–	0.00036	17.11
	−50%	PID	0.00122	0.00547	16.42	0.00069	0.00422	19.66	0.00018	0.00121	23.09
		TID	0.00076	0.00458	15.29	0.00101	0.00369	18.64	–	0.00107	22.21
		FOTID	0.00073	0.00331	13.11	0.00073	0.00337	17.77	–	0.00084	17.55
		FOTIDA	0.00011	0.00142	13.01	0.00014	0.00096	16.99	–	0.00035	17.40
R	+50%	PID	0.00091	0.00546	20.22	0.00053	0.00386	18.29	0.00005	0.00117	19.89
		TID	0.00049	0.00503	18.20	0.00064	0.00361	16.52	0.00001	0.00114	18.91
		FOTID	0.00067	0.00368	17.72	0.00065	0.00338	14.78	0.000007	0.00088	17.83
		FOTIDA	–	0.00150	15.41	0.00012	0.00094	14.01	0.000001	0.00036	15.49
	−50%	PID	0.00074	0.00544	19.53	0.00027	0.00372	20.17	0.00005	0.00111	19.89
		TID	0.00028	0.00475	18.72	0.00041	0.00312	19.11	–	0.00098	19.23
		FOTID	0.00043	0.00356	15.11	0.00051	0.00304	16.77	–	0.00077	18.10
		FOTIDA	–	0.00148	14.33	0.00012	0.00089	15.06	–	0.00034	15.65
B	+50%	PID	0.00086	0.00598	21.01	0.00047	0.00293	21.03	0.00006	0.00131	18.25
		TID	0.00027	0.00374	19.10	0.00041	0.00228	20.89	–	0.00095	18.26
		FOTID	0.00042	0.00270	18.33	0.00040	0.00218	19.32	–	0.00075	17.29
		FOTIDA	0.00004	0.00108	17.43	0.00008	0.00059	19.09	–	0.00032	16.05
	−50%	PID	0.00151	0.00847	20.81	0.00112	0.00763	20.04	0.00006	0.00137	19.48
		TID	0.00059	0.00736	20.33	0.00057	0.00625	18.90	0.00003	0.00135	19.93
		FOTID	0.00086	0.00562	19.05	0.00080	0.00586	18.44	–	0.00105	17.80
		FOTIDA	0.00017	0.00249	18.90	0.00019	0.00177	18.49	–	0.00041	15.12

6. Conclusions

Incorporating renewable energy sources (RESs) and electric vehicles (EVs) into the power grid without adequate control can lead to frequency variations, risking synchronization and destabilizing the utility grid. Numerous load frequency control (LFC) approaches have been discussed in the literature to maintain system frequency stability. However, gaps remain in effectively managing the diverse energy sources within a single region. This paper addresses these gaps by proposing a novel controller design based on fractional order, intended as a centralized single-stage LFC. The TFOID-Accelerated controller is designed to neutralize disturbances from both generation and load, enhancing the stability of multi-microgrids in power imbalance scenarios. Additionally, the paper introduces a recent GO optimization algorithm to fine-tune the TFOID-Accelerated controller's parameters for the interconnected areas under study.

The efficiency of the controller and the optimization technique are validated through simulation results involving various generation settings for PV power plants, as well as diverse generation and load scenarios for wind turbine (WT) systems. The simulations demonstrate the controller's precision and effectiveness in managing frequency disturbances and maintaining grid stability, even with abrupt variations in PV and WT outputs and loads. For example, the proposed controller achieves an approximately 50% reduction in the frequency peak undershoot compared to the best of the other controllers (TID). In scenario 2, with two-step load perturbations (2SLP), the proposed controller significantly reduces frequency undershoots and power fluctuations by nearly 60% compared to the best of the other controllers.

Future research will focus on applying this controller and the enhanced optimization algorithm to different power system case studies, including various generation units, energy storage systems, and load variations. This will help to evaluate further the controller's effectiveness and adaptability in diverse real-world scenarios.

Author Contributions: Conceptualization, M.A. (Mohamed Abdelkader), E.M.A., M.A. (Mokhtar Aly) and Y.S.A.; methodology, M.A. (Mohamed Abdelkader), E.A.M. and M.A. (Mokhtar Aly); software, M.A. (Mohamed Abdelkader), E.M.A., A.A. and S.K.; validation, M.A. (Mohamed Abdelkader), E.A.M. and Y.S.A.; formal analysis, M.A. (Mokhtar Aly), E.M.A. and A.A.; investigation, M.A. (Mohamed Abdelkader), E.A.M. and S.K.; resources, E.M.A., A.A. and Y.S.A.; data curation, E.M.A., Y.S.A., S.K. and F.J.; writing—original draft preparation, M.A. (Mohamed Abdelkader), M.A. (Mokhtar Aly) and S.K.; writing—review and editing, E.A.M., A.A., S.K. and L.N.; visualization, E.A.M. and M.A. (Mokhtar Aly); supervision, S.K., F.J. and L.N.; project administration, A.A., F.J. and L.N.; funding acquisition, Y.S.A., F.J. and L.N. All authors have read and agreed to the published version of the manuscript.

Funding: This research was funded by the Deanship of Graduate Studies and Scientific search at Jouf University under grant No. (DGSSR-2023-02-02445), and ANID, Chile FONDECYT Iniciacion 11230430, and SERC-Chile ANID/FONDAP/1523A0006.

Data Availability Statement: The original contributions presented in the study are included in the article, further inquiries can be directed to the corresponding author.

Conflicts of Interest: Emad A. Mohamed is an employee of Aswan Wireless Communications Research Center (AWCRC). The paper reflects the views of the scientists, and not the company.

References

1. Faheem, M.; Kuusniemi, H.; Eltahawy, B.; Bhutta, M.S.; Raza, B. A lightweight smart contracts framework for blockchain-based secure communication in smart grid applications. *IET Gener. Transm. Distrib.* **2024**, *18*, 625–638. [CrossRef]
2. Das, D.C.; Roy, A.; Sinha, N. GA based frequency controller for solar thermal–diesel–wind hybrid energy generation/energy storage system. *Int. J. Electr. Power Energy Syst.* **2012**, *43*, 262–279. [CrossRef]
3. Zeynali, S.; Rostami, N.; Feyzi, M. Multi-objective optimal short-term planning of renewable distributed generations and capacitor banks in power system considering different uncertainties including plug-in electric vehicles. *Int. J. Electr. Power Energy Syst.* **2020**, *119*, 105885. [CrossRef]
4. Blaabjerg, F.; Yang, Y.; Kim, K.A.; Rodriguez, J. Power Electronics Technology for Large-Scale Renewable Energy Generation. *Proc. IEEE* **2023**, *111*, 335–355. [CrossRef]
5. Zografos, D.; Ghandhari, M. Power system inertia estimation by approaching load power change after a disturbance. In Proceedings of the 2017 IEEE Power & Energy Society General Meeting, Chicago, IL, USA, 16–20 July 2017; pp. 1–5. [CrossRef]
6. Tielens, P.; Van Hertem, D. The relevance of inertia in power systems. *Renew. Sustain. Energy Rev.* **2016**, *55*, 999–1009. [CrossRef]
7. International Energy Agency. Renewables 2022: Analysis and Forecast to 2027. 2023. Available online: https://www.iea.org/reports/renewables-2022 (accessed on 19 May 2023).
8. Smith, C.; Burrows, J.; Scheier, E.; Young, A.; Smith, J.; Young, T.; Gheewala, S.H. Comparative Life Cycle Assessment of a Thai Island's diesel/PV/wind hybrid microgrid. *Renew. Energy* **2015**, *80*, 85–100. [CrossRef]
9. Tripathi, S.; Singh, V.P.; Kishor, N.; Pandey, A. Load frequency control of power system considering electric Vehicles' aggregator with communication delay. *Int. J. Electr. Power Energy Syst.* **2023**, *145*, 108697. [CrossRef]

10. Hosseini, S.A. Frequency control using electric vehicles with adaptive latency compensation and variable speed wind turbines using modified virtual inertia controller. *Int. J. Electr. Power Energy Syst.* **2024**, *155*, 109535. [CrossRef]
11. Amir, M.; Zaheeruddin; Haque, A.; Bakhsh, F.I.; Kurukuru, V.S.B.; Sedighizadeh, M. Intelligent energy management scheme-based coordinated control for reducing peak load in grid-connected photovoltaic-powered electric vehicle charging stations. *IET Gener. Transm. Distrib.* **2023**, *18*, 1205–1222. [CrossRef]
12. Liang, J.; Feng, J.; Fang, Z.; Lu, Y.; Yin, G.; Mao, X.; Wu, J.; Wang, F. An Energy-Oriented Torque-Vector Control Framework for Distributed Drive Electric Vehicles. *IEEE Trans. Transp. Electrif.* **2023**, *9*, 4014–4031. [CrossRef]
13. Liang, J.; Wang, F.; Feng, J.; Zhao, M.; Fang, R.; Pi, D.; Yin, G. A Hierarchical Control of Independently Driven Electric Vehicles Considering Handling Stability and Energy Conservation. *IEEE Trans. Intell. Veh.* **2024**, *9*, 738–751. [CrossRef]
14. Choudhary, R.; Rai, J.; Arya, Y. FOPTID1 controller with capacitive energy storage for AGC performance enrichment of multi-source electric power systems. *Electr. Power Syst. Res.* **2023**, *221*, 109450. [CrossRef]
15. Saikia, L.; Nanda, J.; Mishra, S. Performance comparison of several classical controllers in AGC for multi-area interconnected thermal system. *Int. J. Electr. Power Energy Syst.* **2011**, *33*, 394–401. [CrossRef]
16. Raju, M.; Saikia, L.; Sinha, N. Automatic generation control of a multi-area system using ant lion optimizer algorithm based PID plus second order derivative controller. *Int. J. Electr. Power Energy Syst.* **2016**, *80*, 52–63. [CrossRef]
17. Ali, E.; Abd-Elazim, S. Bacteria foraging optimization algorithm based load frequency controller for interconnected power system. *Int. J. Electr. Power Energy Syst.* **2011**, *33*, 633–638. [CrossRef]
18. Hasan, N.; Alsaidan, I.; Sajid, M.; Khatoon, S.; Farooq, S. Robust self tuned AGC controller for wind energy penetrated power system. *Ain Shams Eng. J.* **2022**, *13*, 101663. [CrossRef]
19. Almasoudi, F.; Bakeer, A.; Magdy, G.; Alatawi, K.; Shabib, G.; Lakhouit, A.; Alomrani, S. Nonlinear coordination strategy between renewable energy sources and fuel cells for frequency regulation of hybrid power systems. *Ain Shams Eng. J.* **2023**, *15*, 102399. [CrossRef]
20. Khalil, A.; Boghdady, T.; Alham, M.; Ibrahim, D. Enhancing the conventional controllers for load frequency control of isolated microgrids using proposed multi-objective formulation via artificial rabbits optimization algorithm. *IEEE Access* **2023**, *11*, 3472–3493. [CrossRef]
21. Bakeer, M.; Magdy, G.; Bakeer, A.; Aly, M. Resilient virtual synchronous generator approach using DC-link capacitor energy for frequency support of interconnected renewable power systems. *J. Energy Storage* **2023**, *65*, 107230. [CrossRef]
22. Taher, S.; Fini, M.; Aliabadi, S. Fractional order PID controller design for LFC in electric power systems using imperialist competitive algorithm. *Ain Shams Eng. J.* **2014**, *5*, 121–135. [CrossRef]
23. Khamari, D.; Sahu, R.; Gorripotu, T.; Panda, S. Automatic generation control of power system in deregulated environment using hybrid TLBO and pattern search technique. *Ain Shams Eng. J.* **2020**, *11*, 553–573. [CrossRef]
24. Guha, D.; Roy, P.; Banerjee, S. Maiden application of SSA-optimised CC-TID controller for load frequency control of power systems. *IET Gener. Transm. Distrib.* **2019**, *13*, 1110–1120. [CrossRef]
25. Elmelegi, A.; Mohamed, E.; Aly, M.; Ahmed, E.; Mohamed, A.A.; Elbaksawi, O. Optimized tilt fractional order cooperative controllers for preserving frequency stability in renewable energy-based power systems. *IEEE Access* **2021**, *9*, 8261–8277. [CrossRef]
26. Mohamed, E.; Ahmed, E.; Elmelegi, A.; Aly, M.; Elbaksawi, O.; Mohamed, A.A. An optimized hybrid fractional order controller for frequency regulation in multi-area power systems. *IEEE Access* **2020**, *8*, 213899–213915. [CrossRef]
27. Ahmed, E.; Mohamed, E.; Elmelegi, A.; Aly, M.; Elbaksawi, O. Optimum modified fractional order controller for future electric vehicles and renewable energy-based interconnected power systems. *IEEE Access* **2021**, *9*, 29993–30010. [CrossRef]
28. Khadanga, R.; Kumar, A.; Panda, S. A modified grey wolf optimization with cuckoo search algorithm for load frequency controller design of hybrid power system. *Appl. Soft Comput.* **2022**, *124*, 109011. [CrossRef]
29. Singh, K.; Arya, Y. Jaya-ITDF control strategy-based frequency regulation of multimicrogrid utilizing energy stored in high-voltage direct current-link capacitors. *Soft Comput.* **2023**, *27*, 5951–5970. [CrossRef]
30. Almasoudi, F.; Magdy, G.; Bakeer, A.; Alatawi, K.; Rihan, M. A new load frequency control technique for hybrid maritime microgrids: Sophisticated structure of fractional-order PIDA controller. *Fractal Fract.* **2023**, *7*, 435. [CrossRef]
31. Zaid, S.; Bakeer, A.; Magdy, G.; Albalawi, H.; Kassem, A.; El-Shimy, M.; AbdelMeguid, H.; Manqarah, B. A new intelligent fractional-order load frequency control for interconnected modern power systems with virtual inertia control. *Fractal Fract.* **2023**, *7*, 62. [CrossRef]
32. Kumari, S.; Shankar, G. Novel application of integral-tilt-derivative controller for performance evaluation of load frequency control of interconnected power system. *IET Gener. Transm. Distrib.* **2018**, *12*, 3550–3560. [CrossRef]
33. Barakat, M. Novel chaos game optimization tuned-fractional-order PID fractional-order PI controller for load–frequency control of interconnected power systems. *Prot. Control. Mod. Power Syst.* **2022**, *7*. [CrossRef]
34. Prakash, A.; Kumar, K.; Parida, S. PIDF(1+FOD) controller for load frequency control with SSSC and AC–DC tie-line in deregulated environment. *IET Gener. Transm. Distrib.* **2020**, *14*, 2751–2762. [CrossRef]
35. Khokhar, B.; Dahiya, S.; Parmar, K. A novel fractional order proportional integral derivative plus second-order derivative controller for load frequency control. *Int. J. Sustain. Energy* **2020**, *40*, 235–252. [CrossRef]
36. Arya, Y. AGC of PV-thermal and hydro-thermal power systems using CES and a new multi-stage FPIDF-(1PI) controller. *Renew. Energy* **2019**, *134*, 796–806. [CrossRef]

37. Guha, D.; Roy, P.; Banerjee, S. Disturbance observer aided optimised fractional-order three-degree-of-freedom tilt-integral-derivative controller for load frequency control of power systems. *IET Gener. Transm. Distrib.* **2020**, *15*, 716–736. [CrossRef]
38. Chinta, D.; Jatoth, R.; Biswal, M. Power system frequency profile improvement using satin bowerbird optimized tilt fractional cascade controller with reduced data based cost function. *J. Eng. Res.* **2023**, *11*, 100116. [CrossRef]
39. Jena, N.; Sahoo, S.; Sahu, B.; Naik, A.; Bajaj, M.; Misak, S.; Blazek, V.; Prokop, L. Impact of a redox flow battery on the frequency stability of a five-area system integrated with renewable sources. *Energies* **2023**, *16*, 5540. [CrossRef]
40. Ahmed, N.; Ebeed, M.; Magdy, G.; Sayed, K.; Gamoura, S.; Metwally, A.; Mahmoud, A.A. A new optimized FOPIDA-FOIDN controller for the frequency regulation of hybrid multi-area interconnected microgrids. *Fractal Fract.* **2023**, *7*, 666. [CrossRef]
41. Rangi, S.; Jain, S.; Arya, Y. scpSSA/scp-optimized cascade scpoptimal-PIDN/scp controller for multi-area power system with scpRFB/scp under deregulated environment. *Optim. Control. Appl. Methods* **2022**, *44*, 1972–1994. [CrossRef]
42. Babu, N.; Bhagat, S.; Chiranjeevi, T.; Pushkarna, M.; Saha, A.; Kotb, H.; AboRas, K.; Alsaif, F.; Alsulamy, S.; Ghadi, Y.; et al. Frequency control of a realistic dish stirling solar thermal system and accurate HVDC models using a cascaded FOPI-IDDN-based crow search algorithm. *Int. J. Energy Res.* **2023**, *2023*, 9976375. [CrossRef]
43. Noman, A.M.; Aly, M.; Alqahtani, M.H.; Almutairi, S.Z.; Aljumah, A.S.; Ebeed, M.; Mohamed, E.A. Optimum Fractional Tilt Based Cascaded Frequency Stabilization with MLC Algorithm for Multi-Microgrid Assimilating Electric Vehicles. *Fractal Fract.* **2024**, *8*, 132. [CrossRef]
44. Dahab, Y.A.; Abubakr, H.; Mohamed, T.H. Adaptive Load Frequency Control of Power Systems Using Electro-Search Optimization Supported by the Balloon Effect. *IEEE Access* **2020**, *8*, 7408–7422. [CrossRef]
45. Ewais, A.M.; Elnoby, A.M.; Mohamed, T.H.; Mahmoud, M.M.; Qudaih, Y.; Hassan, A.M. Adaptive frequency control in smart microgrid using controlled loads supported by real-time implementation. *PLoS ONE* **2023**, *18*, e0283561. [CrossRef]
46. Yousri, D.; Babu, T.S.; Fathy, A. Recent methodology based Harris Hawks optimizer for designing load frequency control incorporated in multi-interconnected renewable energy plants. *Sustain. Energy Grids Netw.* **2020**, *22*, 100352. [CrossRef]
47. Shabani, H.; Vahidi, B.; Ebrahimpour, M. A robust PID controller based on imperialist competitive algorithm for load-frequency control of power systems. *ISA Trans.* **2013**, *52*, 88–95. [CrossRef]
48. El Yakine Kouba, N.; Menaa, M.; Hasni, M.; Boudour, M. Optimal load frequency control based on artificial bee colony optimization applied to single, two and multi-area interconnected power systems. In Proceedings of the 2015 3rd International Conference on Control, Engineering & Information Technology (CEIT), Tlemcen, Algeria, 25–27 May 2015; pp. 1–6. [CrossRef]
49. AboRas, K.M.; Ragab, M.; Shouran, M.; Alghamdi, S.; Kotb, H. Voltage and frequency regulation in smart grids via a unique Fuzzy PIDD2 controller optimized by Gradient-Based Optimization algorithm. *Energy Rep.* **2023**, *9*, 1201–1235. [CrossRef]
50. Fathy, A.; Alharbi, A.G. Recent Approach Based Movable Damped Wave Algorithm for Designing Fractional-Order PID Load Frequency Control Installed in Multi-Interconnected Plants with Renewable Energy. *IEEE Access* **2021**, *9*, 71072–71089. [CrossRef]
51. Ayas, M.S.; Sahin, E. FOPID controller with fractional filter for an automatic voltage regulator. *Comput. Electr. Eng.* **2021**, *90*, 106895. [CrossRef]
52. Zaheeruddin; Singh, K. Load frequency regulation by de-loaded tidal turbine power plant units using fractional fuzzy based PID droop controller. *Appl. Soft Comput.* **2020**, *92*, 106338. [CrossRef]
53. Abid, S.; El-Rifaie, A.M.; Elshahed, M.; Ginidi, A.R.; Shaheen, A.M.; Moustafa, G.; Tolba, M.A. Development of Slime Mold Optimizer with Application for Tuning Cascaded PD-PI Controller to Enhance Frequency Stability in Power Systems. *Mathematics* **2023**, *11*, 1796. [CrossRef]
54. Zhang, G.; Daraz, A.; Khan, I.A.; Basit, A.; Khan, M.I.; Ullah, M. Driver Training Based Optimized Fractional Order PI-PDF Controller for Frequency Stabilization of Diverse Hybrid Power System. *Fractal Fract.* **2023**, *7*, 315. [CrossRef]
55. Malik, S.; Suhag, S. A Novel SSA Tuned PI-TDF Control Scheme for Mitigation of Frequency Excursions in Hybrid Power System. *Smart Sci.* **2020**, *8*, 202–218. [CrossRef]
56. Dash, P.; Saikia, L.; Sinha, N. Automatic generation control of multi area thermal system using Bat algorithm optimized PD–PID cascade controller. *Int. J. Electr. Power Energy Syst.* **2015**, *68*, 364–372. [CrossRef]
57. Arya, Y.; Kumar, N.; Dahiya, P.; Sharma, G.; Çelik, E.; Dhundhara, S.; Sharma, M. Cascade-$I^{\lambda}D^{\mu}N$ controller design for AGC of thermal and hydro-thermal power systems integrated with renewable energy sources. *IET Renew. Power Gener.* **2021**, *15*, 504–520. [CrossRef]
58. Sahu, R.; Panda, S.; Rout, U.K.; Sahoo, D. Teaching learning based optimization algorithm for automatic generation control of power system using 2-DOF PID controller. *Int. J. Electr. Power Energy Syst.* **2016**, *77*, 287–301. [CrossRef]
59. Oshnoei, S.; Aghamohammadi, M.; Oshnoei, S.; Oshnoei, A.; Mohammadi-Ivatloo, B. Provision of Frequency Stability of an Islanded Microgrid Using a Novel Virtual Inertia Control and a Fractional Order Cascade Controller. *Energies* **2021**, *14*, 4152. [CrossRef]
60. El-Sousy, F.F.M.; Aly, M.; Alqahtani, M.H.; Aljumah, A.S.; Almutairi, S.Z.; Mohamed, E.A. New Cascaded 1+PII2D/FOPID Load Frequency Controller for Modern Power Grids including Superconducting Magnetic Energy Storage and Renewable Energy. *Fractal Fract.* **2023**, *7*, 672. [CrossRef]
61. Micev, M.; Ćalasan, M.; Oliva, D. Fractional Order PID Controller Design for an AVR System Using Chaotic Yellow Saddle Goatfish Algorithm. *Mathematics* **2020**, *8*, 1182. [CrossRef]
62. Dulf, E.H. Simplified Fractional Order Controller Design Algorithm. *Mathematics* **2019**, *7*, 1166. [CrossRef]

63. Motorga, R.; Mureșan, V.; Ungureșan, M.L.; Abrudean, M.; Vălean, H.; Clitan, I. Artificial Intelligence in Fractional-Order Systems Approximation with High Performances: Application in Modelling of an Isotopic Separation Process. *Mathematics* **2022**, *10*, 1459. [CrossRef]
64. Zhang, Q.; Gao, H.; Zhan, Z.H.; Li, J.; Zhang, H. Growth Optimizer: A powerful metaheuristic algorithm for solving continuous and discrete global optimization problems. *Knowl.-Based Syst.* **2023**, *261*, 110206. [CrossRef]
65. Fatani, A.; Dahou, A.; Abd Elaziz, M.; Al-qaness, M.A.A.; Lu, S.; Alfadhli, S.A.; Alresheedi, S.S. Enhancing Intrusion Detection Systems for IoT and Cloud Environments Using a Growth Optimizer Algorithm and Conventional Neural Networks. *Sensors* **2023**, *23*, 4430. [CrossRef] [PubMed]
66. Aribia, H.B.; El-Rifaie, A.M.; Tolba, M.A.; Shaheen, A.; Moustafa, G.; Elsayed, F.; Elshahed, M. Growth Optimizer for Parameter Identification of Solar Photovoltaic Cells and Modules. *Sustainability* **2023**, *15*, 7896. [CrossRef]